ELSEVIER

International Journal of Solids and Structures 41 (2004) 3053–3080

INTERNATIONAL JOURNAL OF SOLIDS and STRUCTURES

www.elsevier.com/locate/ijsolstr

Identification and applications of boundary effects in beams

P. Frank Pai [a,*], Lu Huang [a], Sharath H. Gopalakrishnamurthy [a], Jaycee H. Chung [b]

[a] *Department of Mechanical and Aerospace Engineering, University of Missouri-Columbia, E2403C Engineering Building East, Columbia, MO 65211, USA*

[b] *Global Contour Inc., Rockwall, TX 75087, USA*

Received 8 July 2003; received in revised form 5 January 2004

Available online 5 March 2004

Abstract

Presented here is a signal decomposition method for extracting boundary effects from an operational deflection shape (ODS) of a structure under harmonic excitation. It decomposes an ODS into central and boundary solutions using a sliding-window least-squares curve-fitting technique, and the boundary solutions can be used to reveal damage locations, and the central solutions can be used to identify boundary conditions. Except an experimental ODS the method requires no model or historical data for comparison. Exact mode shapes and ODSs of beams with damage are obtained by spectral element analysis. Boundary and central solutions caused by different boundary conditions, different loading conditions, and different damage with or without noise are simulated and characterized. Numerical results show that Gibbs' phenomenon caused by the use of continuously differential functions to fit ODSs with discontinuous first-, second-, and/or third-order derivatives actually makes boundary solutions excellent damage indicators. Several experiments are performed using a scanning laser vibrometer for sensing and a lead zirconate titanate (PZT) patch for actuation. The experimental results confirm the feasibility and accuracy of this boundary effect detection method in detecting multiple defects and identifying boundary conditions of beams.

Keywords: Identification of defects and boundaries; Operational deflection shapes; Boundary effects; Scanning laser vibrometer

1. Introduction

Several dynamics-based structural health monitoring methods have shown the capability of detecting the existence of defects in structures (Doebling et al., 1996). However, locating and estimating defects in structures remains a challenging issue, especially locating small defects without historical data or an accurate structural model with known boundary conditions.

It is well known in the literature that using structural dynamic responses to locate small defects requires the use of high-frequency deflection shapes, i.e., deflection shapes with high local curvatures. Unfortunately,

* Corresponding author. Tel.: +1-573-884-1474; fax: +1-573-884-5090.
E-mail address: paip@missouri.edu (P.F. Pai).

0020-7683/$ - see front matter © 2004 Elsevier Ltd. All rights reserved.
doi:10.1016/j.ijsolstr.2004.01.020

to obtain high-frequency deflection shapes requires spatially dense and accurate measurements in order to reduce spatial aliasing in signal processing. A scanning laser vibrometer provides a unique solution to the spatial aliasing problem because of its non-contact, remote, large-area scanning, dense, high-frequency bandwidth, and accurate measurement capabilities. However, even if a scanning laser vibrometer is available, how to extract clear damage signals from the large amount of dynamic response data obtained from a scanning laser vibrometer is another challenging issue.

Actual boundary conditions of a built-up structure are usually difficult to determine (Wang and Chen, 1996; Lee and Jeon, 1999). Even for some simple structures it is difficult to determine appropriate boundary conditions. For example, a simply supported boundary of a beam is difficult to be realized in experiment. The simply supported boundary becomes similar to a clamped end if the supporting force is too large, and sliding and jumping with friction becomes a difficult non-linear problem if the supporting force is too small. A clamped end is usually considered to be easy to setup in experiment. But, if the clamping force is too large, the boundary effects deviate significantly from the ideal ones because of cross section warpings. Moreover, sometimes boundary points of a structure are not accessible or only a few points close to a boundary can be measured. Hence, identification of actual boundaries of an existing structure is important and challenging. However, very few studies have been performed on the identification of actual boundary conditions although it is important in the assessment of aging structures or structures after natural disasters (e.g., earthquakes and tornados).

Pai and Jin (2000) derived a boundary effect detection (BED) method that can locate small structural defects by using operational deflection shapes (ODSs) measured by a scanning laser vibrometer. The BED method works without using historical data; it uses a sliding-window least-squares curve-fitting technique to extract boundary solutions from an ODS to reveal defect locations. Experiments have been performed to verify the capability of the BED method in locating surface slots, edge slots, surface holes, internal holes, fatigue cracks, and stiffened sections (Pai and Jin, 2000; Pai and Young, 2001; Jin and Pai, 2000). Numerical and experimental results show that the BED method seems more sensitive and reliable than other dynamics- or deformation-based methods. However, some questions about the BED method remain to be answered and some limitations need to be eliminated.

This work is (1) to explain why the damage detection curves obtained from the BED method show certain strong characters that can be used to reveal multiple damage locations, (2) to extend the BED method for detecting defects around boundaries and for identifying structural boundary conditions, and (3) to experimentally verify this improved BED method.

2. Measurement of operational deflection shapes

Fig. 1 shows the experimental setup used in measuring ODSs of a structure. An ODS is defined in this work as the deflection shape of a structure when it is subjected to a single-point or multiple-point or distributed harmonic excitation at one frequency. A Polytec PSV-200 scanning laser vibrometer is used to measure the velocities of equally spaced points over the structure when the structure is subjected to a harmonic excitation from an actuator, such as a lead zirconate titanate (PZT) patch integrated with the structure (as shown in Fig. 1) or an external electromechanical shaker. The PZT patch used here is a QuickPack QP10N actuator purchased from ACX, Inc. The QuickPack actuator packages piezoceramics in a protective polyimide coating with pre-attached electrical leads. It is a $2'' \times 1'' \times 0.015''$ patch with a $1.81'' \times 0.81'' \times 0.010''$ piezo wafer, and the maximum allowable operating voltage is 200 V.

The PCB-790 power amplifier magnifies, by 20 times, the sinusoidal voltage from the HP-33120A 15 MHz function generator and sends it to the PZT patch. The OFV-3001-S vibrometer controller controls the rotation of the two mirrors in the OFV-055 scan head and the scanning of the laser beam, and it receives the interferometry created by the backscattered laser beam and the reference laser beam in the OFV-303 sensor

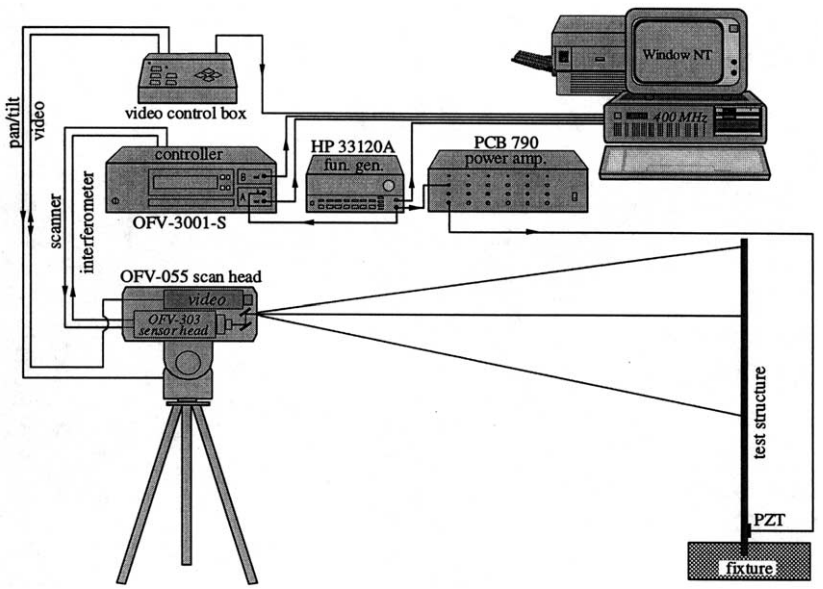

Fig. 1. The experimental setup for measuring ODSs of a structure using a PSV-200 scanning laser vibrometer for sensing and a PZT patch for actuation.

head. The output voltage from the HP-33120A function generator is also used as the input signal to Channel A of the OFV-3001-S vibrometer controller. The OFV-3001-S controller includes two independently programmable low-pass filters for filtering the signal from the HP-33120A function generator and the signal from the OFV-303 sensor head, respectively. After filtering, these two signals are sent from Channels A and B of the controller to the 400 MHz computer system, which is operated by the Windows NT and processes the measured data. The video control box controls the swiveling and tilting of the OFV-055 scan head and the focusing of the video camera in the OFV-055 scan head. A standardized composite video signal from the camera is passed via a BNC connection on the video control box to the video input of the computer system.

To obtain experimental ODSs we first perform an "FFT" acquisition to obtain frequency response functions (FRFs) of all measurement points using a periodic chirp excitation, and then we choose an isolated natural frequency or any other frequency from the averaged FRF. After that we perform a "FAST SCAN" acquisition using a single-frequency excitation at the chosen frequency to obtain the corresponding ODS.

The noise level of the measured ODSs is primary determined by the frequency bandwidth B_w used in the "FAST SCAN" acquisition. The noise level is proportional to $\sqrt{B_w}$. However, the minimum bandwidth is limited to 0.02% of the excitation frequency, and the data acquisition time increases when B_w decreases. Hence the noise level of high-frequency ODSs obtained using the "FAST SCAN" acquisition can be high. However, the noise level of all ODSs obtained in this study is estimated to have a standard deviation below 0.1% of the maximum value of the corresponding ODS.

The velocity profile obtained from a scanning laser vibrometer is based on the assumption that the vibration period of each measurement point is the same. If the vibration is periodic with a known period T and the recording at each location is triggered to start at nT (n is an integer) after the beginning recording time of the previous measurement point, the velocity profile at $t = t_k$ can be obtained by connecting the measured velocities of all measurement points at t_k. If the vibration consists of harmonics that are not

commensurable or unknown non-linear coupling exists, the ODS cannot be measured using a scanning laser vibrometer because the period T is unknown. For such cases, one need to use a 3D motion analysis system, which measure the instant locations of all measurement points simultaneously and hence the obtained ODSs are the true ODSs. However, the maximum number of measurement points of such systems is limited and the maximum sampling frequency is 2000 Hz or less. Hence, high-order ODSs cannot be measured using such systems.

3. Analysis of imperfect beams

Here we show how to obtain numerical dynamic characteristics of a beam with damage and/or imperfect boundary conditions. Fig. 2(a) shows a beam having a rectangular cross section, a symmetric open crack at $x = a$, and clamped-supported boundary conditions. If the beam is modeled as three beam segments, the corresponding equation of motion can be derived to be

$$[E\tilde{I}w'']'' + \tilde{c}\dot{w} + \tilde{m}\ddot{w} = f(x,t) \tag{1}$$

where

$$\begin{aligned} &\tilde{I} \equiv I - \hat{I}[u(x-a) - u(x-a-c)], \quad \hat{I} \equiv 2\int_{h/2-e}^{h/2} z^2 \,\mathrm{d}A \\ &\tilde{m} \equiv m - \hat{m}[u(x-a) - u(x-a-c)], \quad \hat{m} \equiv 2em/h \end{aligned} \tag{2}$$

And, boundary conditions are given by

$$w(0,t) = w'(0,t) = 0, \qquad \tau_1 w(L,t) - EIw'''(L,t) = 0, \qquad \tau_2 w'(L,t) + EIw''(L,t) = 0 \tag{3}$$

Here w is the transverse displacement, E Young's modulus, I the area moment of inertia of the intact beam, $I - \hat{I}(\equiv I_1)$ the area moment of inertia of the slotted segment, $\tilde{m}$ the mass per unit length, $\tilde{c}$ the damping coefficient, $w' \equiv \partial w/\partial x$, $\dot{w} \equiv \partial w/\partial t$, t the time, A the cross sectional area, $u(x-a)$ a unit step function, h the beam thickness, b the beam width, e the crack depth, c the crack width, and $f(x,t)$ is the distributed external

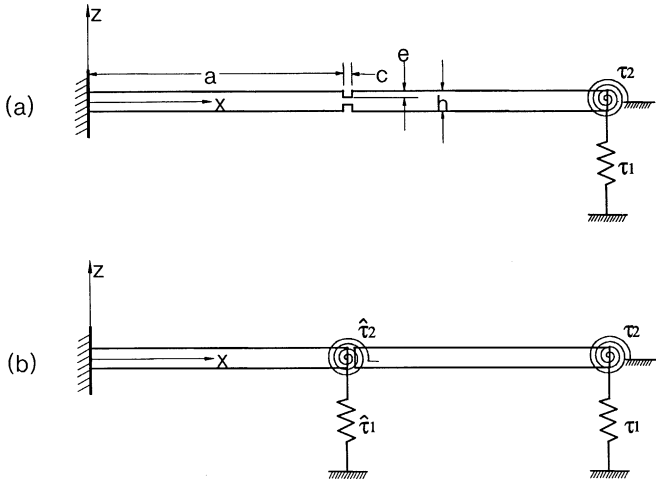

Fig. 2. A clamped-supported beam with a symmetric open crack: (a) the system and (b) a simplified model.

load. Moreover, L is the beam length, τ_1 is the linear spring constant, and τ_2 is the torsional spring constant of the springs at $x = L$. Eq. (1) can be rewritten as

$$EIw^{iv} + \tilde{c}\dot{w} + \tilde{m}\ddot{w} = E\hat{I}w''[u''(x-a) - u''(x-a-c)] + 2E\hat{I}w'''[u'(x-a) - u'(x-a-c)] + E\hat{I}w^{iv}[u(x-a) - u(x-a-c)] + f(x,t) \tag{4}$$

Because $u'(x-a) = \delta(x-a)$ (the Kronecker delta function) and $u''(x-a) = \delta'(x-a)$, Eq. (4) shows that the forced damped vibration of a beam with a slot is equivalent to an intact beam subjected to two concentrated bending moments $E\hat{I}w''(a^+)$ and $-E\hat{I}w''(a+c^-)$, two concentrated shear forces $2E\hat{I}w'''(a^+)$ and $-2E\hat{I}w'''(a+c^-)$, one distributed force $E\hat{I}w^{iv}$ between $x = a$ and $x = a + c$, and the externally applied distributed load $f(x,t)$ (Thomson, 1949; Man et al., 1994).

3.1. Dynamic characteristics

The ith mode shape ϕ_i is the free undamped deflection shape harmonically vibrating at the ith natural frequency ω_i and is given by

$$\phi_i(x) = \bar{c}_1 \cos\beta_i x + \bar{c}_2 \sin\beta_i x + \bar{c}_3 \cosh\beta_i x + \bar{c}_4 \sinh\beta_i x, \quad \beta_i \equiv \left(\frac{m\omega_i^2}{EI}\right)^{1/4} \tag{5}$$

where the coefficients $\bar{c}_i$ are determined by boundary conditions and β_i is determined by the corresponding frequency equation. To obtain ϕ_i and ω_i one can model the damaged beam shown in Fig. 2(a) as three beam segments and use boundary conditions and the continuity of displacements, slopes, bending moments, and shear forces at the two joints. If the $\phi_i(x)$ is normalized with respect to $\tilde{m}$ to be

$$\int_0^L \tilde{m}\phi_i^2(x)\,\mathrm{d}x = 1, \tag{6}$$

the FRF H_{mn} for the response $w(x_m,t)(= W(x_m)\,\mathrm{e}^{\mathrm{j}\Omega t})$ due to a harmonic excitation $f(x,t) = F_0\delta(x-x_n)\,\mathrm{e}^{\mathrm{j}\Omega t}$ can be derived to be (Inman, 2001)

$$H_{mn}(\Omega) = \frac{W(x_m)}{F_0} = \sum_{i=1}^{\infty} \frac{\phi_i(x_m)\phi_i(x_n)}{\omega_i^2 - \Omega^2 + 2\zeta_i\omega_i\Omega\mathrm{j}} \tag{7}$$

where Ω is the excitation frequency, $\mathrm{j} \equiv \sqrt{-1}$, and ζ_i is the modal damping ratio for the ith mode. However, this is an indirect approach because all mode shapes and natural frequencies need to be obtained first and a summation of infinite terms is needed. Another way to obtain FRFs is to derive a finite element model first and then use the obtained mass ($[M]$), damping ($[C]$), and stiffness ($[K]$) matrices to compute the FRF matrix $[H]$ as $[H] = [-\Omega^2[M] + \mathrm{j}\Omega[C] + [K]]^{-1}$. However, this approach is also indirect and it is not accurate in predicting high-frequency FRFs, bending moments, and shear forces because of the approximate, polynomial shape functions used in finite element modeling. Hence we are going to use the spectral element method (Doyle, 1989; Lee and Lee, 1997, 1999) to obtain natural frequencies and mode shapes and directly compute FRFs and ODSs of beams with damage and/or non-ideal boundary conditions.

An ODS is different from a mode shape. However, if $\tilde{c}$ is constant and $f(x,t) = F(x)\sin(\omega_i t)$ with $F(x) = \phi_i(x)$, the distributed excitation force is exactly balanced out by the distributed damping force and the ODS is the same as the free vibration mode shape ϕ_i. If the beam is subjected to a periodic excitation $f(x,t) = F_0\delta(x-x_n)\,\mathrm{e}^{\mathrm{j}\Omega t}$, $w(x,t) = W(x)\,\mathrm{e}^{\mathrm{j}\Omega t}$. And, for a uniform section of the beam that is free of loads, damage and damping, the ODS $W(x)$ is given by

$$W(x) = c_1 \cos \beta x + c_2 \sin \beta x + c_3 \cosh \beta x + c_4 \sinh \beta x, \beta = \left(\frac{m\Omega^2}{EI} \right)^{1/4} \tag{8}$$

Of course $W(x)$ is a function of Ω also; however, we use $W(x)$ instead of $W(x, \Omega)$ to simplify the expressions. Eqs. (7) and (8) show that

$$W(x) = \sum_{i=1}^{\infty} \frac{F_0 \phi_i(x) \phi_i(x_n)}{\omega_i^2 - \Omega^2} \tag{9}$$

Eqs. (8) and (9) indicate that, when Ω is not close to an isolated natural frequency, the ODS may consist of multiple mode shapes but the ODS is still a normal mode. Experimental results show that, even when $F(x)$ is different from a mode shape but the excitation frequency is close to the ith natural frequency, the ODS is still dominated by the ith mode shape. However, Eqs. (7) and (9) show that, when damping is significant, the ODS is very possible a complex mode if Ω is not close to an isolated natural frequency. In such cases, the ODS actually consists of several mode shapes and the nodes are traveling (Nayfeh and Mook, 1979; Pai and Lee, 2003). If there is no non-linear effects (e.g., non-linear modal coupling and energy transferring to low-frequency modes), the complex mode still vibrates at the excitation frequency Ω but the deflection shape periodically change with time.

3.2. Spectral element analysis

If three two-node beam elements are used to model the beam shown in Fig. 2(a), because $w_1 = w(-l, t)$, $\theta_1 = w'(-l, t)$, $w_2 = w(l, t)$ and $\theta_2 = w'(l, t)$ for the first element, one can use Eq. (8) to derive that,

$$w(x, t) = N_1(x) w_1 + N_2(x) \theta_1 + N_3(x) w_2 + N_4(x) \theta_2 \tag{10a}$$

where $-l \leqslant x \leqslant l$, the elemental beam length is $2l$, and

$$\begin{aligned}
N_1(x) &= \frac{\sinh \beta l \cos \beta x + \sin \beta l \cosh \beta x}{d_1} + \frac{-\cosh \beta l \sin \beta x + \cos \beta l \sinh \beta x}{d_2} \\
N_2(x) &= \frac{\cosh \beta l \cos \beta x - \cos \beta l \cosh \beta x}{\beta d_1} + \frac{-\sinh \beta l \sin \beta x + \sin \beta l \sinh \beta x}{\beta d_2} \\
N_3(x) &= \frac{\sinh \beta l \cos \beta x + \sin \beta l \cosh \beta x}{d_1} + \frac{\cosh \beta l \sin \beta x - \cos \beta l \sinh \beta x}{d_2} \\
N_4(x) &= \frac{-\cosh \beta l \cos \beta x + \cos \beta l \cosh \beta x}{\beta d_1} + \frac{-\sinh \beta l \sin \beta x + \sin \beta l \sinh \beta x}{\beta d_2} \\
d_1 &\equiv 2(\sin \beta l \cosh \beta l + \cos \beta l \sinh \beta l), \qquad d_2 \equiv 2(\sin \beta l \cosh \beta l - \cos \beta l \sinh \beta l)
\end{aligned} \tag{10b}$$

Because the bending moments M_i and shear forces V_i at the left ($i = 1$) and right ($i = 2$) nodes of the first beam element are related to w as

$$V_1 = EIw'''(-l, t), \qquad M_1 = -EIw''(-l, t), \qquad V_2 = -EIw'''(l, t), \qquad M_2 = EIw''(l, t) \tag{11}$$

we obtain from Eqs. (10) and (11) that

$$\begin{Bmatrix} V_1 \\ M_1 \\ V_2 \\ M_2 \end{Bmatrix} = [k] \begin{Bmatrix} w_1 \\ \theta_1 \\ w_2 \\ \theta_2 \end{Bmatrix}, \qquad [k] \equiv \begin{bmatrix} k_{11} & k_{12} & k_{13} & k_{14} \\ k_{12} & k_{22} & k_{23} & k_{24} \\ k_{13} & k_{23} & k_{33} & k_{34} \\ k_{14} & k_{24} & k_{34} & k_{44} \end{bmatrix} \tag{12a}$$

where

$$
\begin{aligned}
k_{11} &= k_{33} \equiv -D_0\beta^2(\cos 2\beta l \sinh 2\beta l + \sin 2\beta l \cosh 2\beta l)\\
k_{12} &= -k_{34} \equiv -D_0\beta \sin 2\beta l \sinh 2\beta l\\
k_{13} &\equiv D_0\beta^2(\sin 2\beta l + \sinh 2\beta l)\\
k_{14} &= -k_{23} \equiv D_0\beta(\cos 2\beta l - \cosh 2\beta l)\\
k_{22} &= k_{44} \equiv D_0(\cos 2\beta l \sinh 2\beta l - \sin 2\beta l \cosh 2\beta l)\\
k_{24} &\equiv D_0(\sin 2\beta l - \sinh 2\beta l)\\
D_0 &\equiv EI\beta/(\cos 2\beta l \cosh 2\beta l - 1)
\end{aligned}
\tag{12b}
$$

The coordinate transformation for transforming the elemental dynamic stiffness matrix $[k]$ and the assembly of global dynamic stiffness matrix $[K]$ are the same as those used in conventional finite element modeling. Both $[k]$ and $[K]$ are symmetric. We note that the $[k]$ will be singular when $\cos 2\beta l \cosh 2\beta l = 1$. In that case, one can choose a different elemental length. Because the beam in Fig. 2(a) is modeled using three elements, we have

$$
\begin{aligned}
&[K]\{q\} = \{F\}\\
&\{q\} \equiv \{w_1, \theta_1, w_2, \theta_2, w_3, \theta_3, w_4, \theta_4\}^{\mathrm{T}}, \qquad \{F\} \equiv \{V_1, M_1, V_2, M_2, V_3, M_3, V_4, M_4\}^{\mathrm{T}}
\end{aligned}
\tag{13}
$$

If the right end of the beam shown in Fig. 2(a) is free, the external forces and moments on the nodes are

$$
V_2 = M_2 = V_3 = M_3 = V_4 = M_4 = 0 \tag{14}
$$

and V_1 and M_1 are unknown. Using the boundary conditions $w_1 = \theta_1 = 0$ to reduce the $[K]$ into a 6×6 matrix $[\overline{K}]$ and then use $|\,[\overline{K}]\,| = 0$ to determine natural frequencies and mode shapes. The FRF matrix $[H]$ can be obtained as $[\overline{K}]^{-1}$.

4. Extraction of boundary effects

To extract boundary effects from an ODS we improve our previous approach (Pai and Jin, 2000) by separating left and right boundary conditions. For an ODS of the entire beam, we have

$$
\begin{aligned}
W(x) &= c_1 \cos\beta x + c_2 \sin\beta x + c_3 \cosh\beta x + c_4 \sinh\beta x\\
&= c_1 \cos\beta x + c_2 \sin\beta x + \hat{c}_3\, \mathrm{e}^{\beta x} + \hat{c}_4\, \mathrm{e}^{-\beta x}, \quad \hat{c}_3 \equiv \frac{c_3 + c_4}{2}, \;\; \hat{c}_4 \equiv \frac{c_3 - c_4}{2}
\end{aligned}
\tag{15}
$$

It is apparent that, when β is large, $\hat{c}_3\, \mathrm{e}^{\beta x} (= \tilde{c}_3\, \mathrm{e}^{-\beta(L-x)}, \tilde{c}_3 \equiv \hat{c}_3\, \mathrm{e}^{\beta L})$ decays toward zero at $x = 0$ and $\hat{c}_4\, \mathrm{e}^{-\beta_i x}$ decays toward zero at $x = L$. Hence, these two terms are right and left boundary solutions, and the first two terms are called central solutions.

For a large structure, measuring an ODS of the entire structure using one measurement setup is difficult, and it is more practical to measure and process the ODS of a local small area at each time. Hence, we will use a sliding-window least-squares curve-fitting method and a moving coordinate $\bar{x}$ ($\equiv x - x_m$, x_m is the location of the point under observation) for processing a local ODS to extract boundary solutions. Hence we rewrite Eq. (15) as

$$
\begin{aligned}
W(\bar{x}) &= c_1\cos(\beta x_m+\beta\bar{x})+c_2\sin(\beta x_m+\beta\bar{x})+c_3\cosh(\beta x_m+\beta\bar{x})+c_4\sinh(\beta x_m+\beta\bar{x})\\
&= C_1\cos(\beta\bar{x})+C_2\sin(\beta\bar{x})+C_3\cosh(\beta\bar{x})+C_4\sinh(\beta\bar{x})\\
&= C_1\cos(\beta\bar{x})+C_2\sin(\beta\bar{x})+\widehat{C}_3\,\mathrm{e}^{\beta\bar{x}}+\widehat{C}_4\,\mathrm{e}^{-\beta\bar{x}}
\end{aligned}
\tag{16}
$$

where

$$
\begin{aligned}
&C_1\equiv\sqrt{c_1^2+c_2^2}\cos(\beta x_m-\phi),\quad C_2\equiv-\sqrt{c_1^2+c_2^2}\sin(\beta x_m-\phi),\quad \tan\phi\equiv\frac{c_2}{c_1}\\
&C_3\equiv\sqrt{c_3^2+c_4^2}\cosh(\beta x_m+\psi),\quad C_4\equiv\sqrt{c_3^2+c_4^2}\sinh(\beta x_m+\psi),\quad \tanh\psi\equiv\frac{c_4}{c_3}\\
&\widehat{C}_3\equiv\frac{C_3+C_4}{2},\quad \widehat{C}_4\equiv\frac{C_3-C_4}{2},\quad C_3=\widehat{C}_3+\widehat{C}_4,\quad C_4=\widehat{C}_3-\widehat{C}_4
\end{aligned}
\tag{17}
$$

To find the coefficients $C_i(i=1,2,3,4)$ for the point at $\bar{x}=0$ (i.e., $x=x_m$) we use the data points around $x=x_m$ to minimize the fitting error. If W_i denotes $W(\bar{x}_i)$ and Y_i denotes the experimental data at $\bar{x}_i$, we define the fitting error E_{rror} as

$$
E_{\mathrm{rror}}\equiv\sum_{i=-N}^{N}\alpha_i(W_i-Y_i)^2 \tag{18}
$$

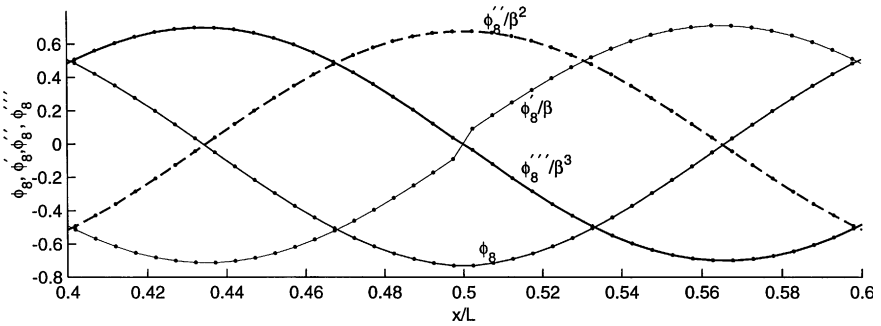

Fig. 3. The eighth mode shape of a $22''\times1''\times0.25''$ cantilever with a crack having $a+c/2=L/2$, $c=0.039''$ and $2e=0.4h$.

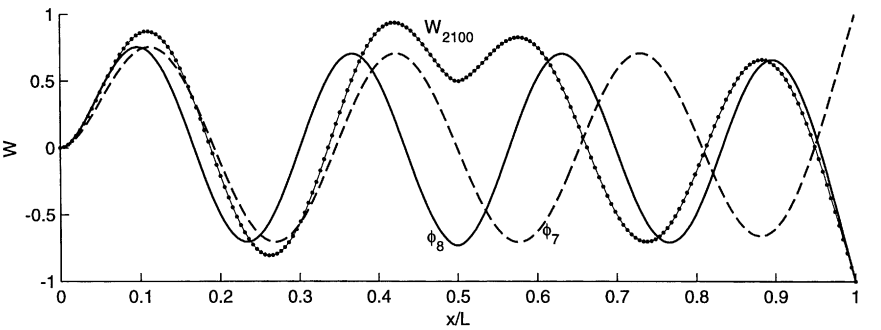

Fig. 4. The 2100 Hz ODS, W_{2100}, and seventh and eighth mode shapes, ϕ_7 and ϕ_8, of the $22''\times1''\times0.25''$ cantilever with a symmetric center crack.

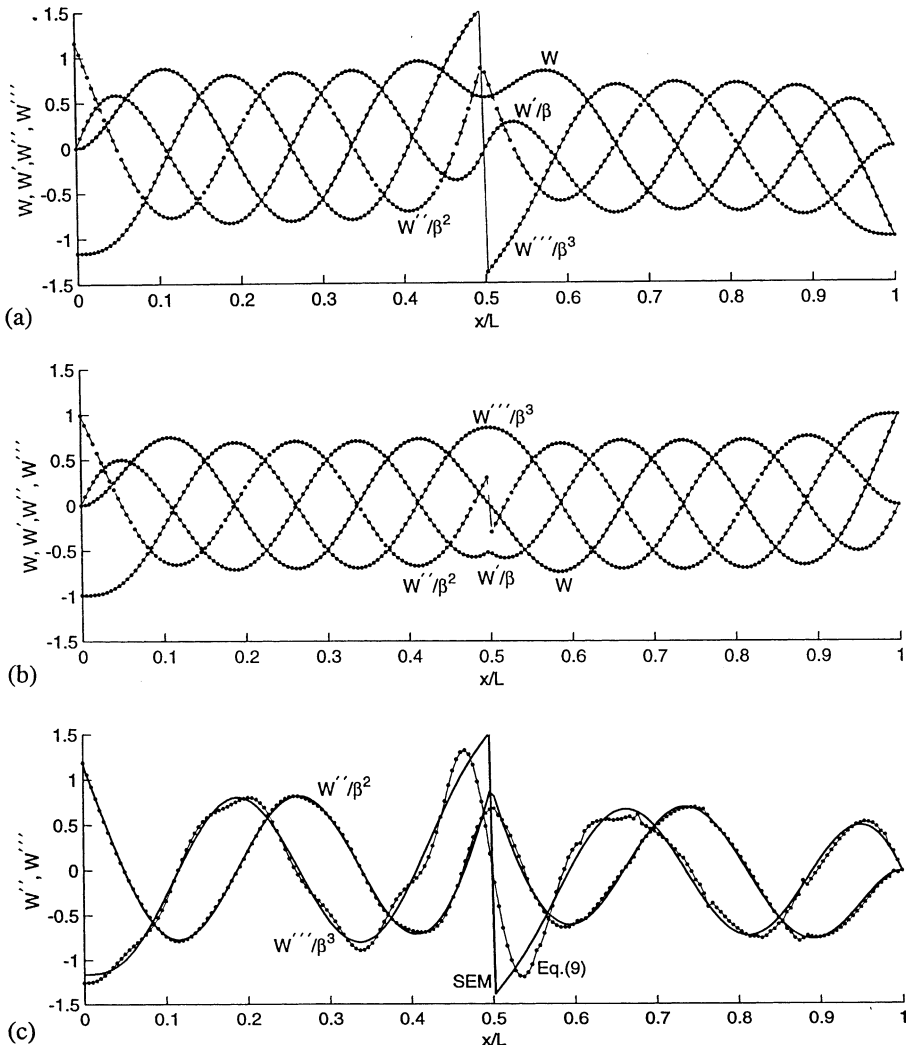

Fig. 5. The 2100 Hz ODS, W, and its derivatives of the $22'' \times 1'' \times 0.25''$ cantilever without crack: (a) an external force at $x = 10.981''$, (b) an external moment at $x = 10.981''$, and (c) ODSs obtained using Eq. (9) (dotted lines) and spectral elements (solid lines) with an external force at $x = 10.981''$.

where the total number of points used is $2N + 1$, and α_i is a weighting factor. In this work, we choose to use

$$\alpha_i = \frac{1}{1 + |99i/N|} \tag{19}$$

The four equations to determine C_i for the point at $\bar{x} = 0$ are given by

$$\frac{\partial E_{\text{rror}}}{\partial C_j} = \sum_{i=-N}^{N} 2\alpha_i (W_i - Y_i) \frac{\partial W_i}{\partial C_j} = 0, \quad j = 1, 2, 3, 4 \tag{20}$$

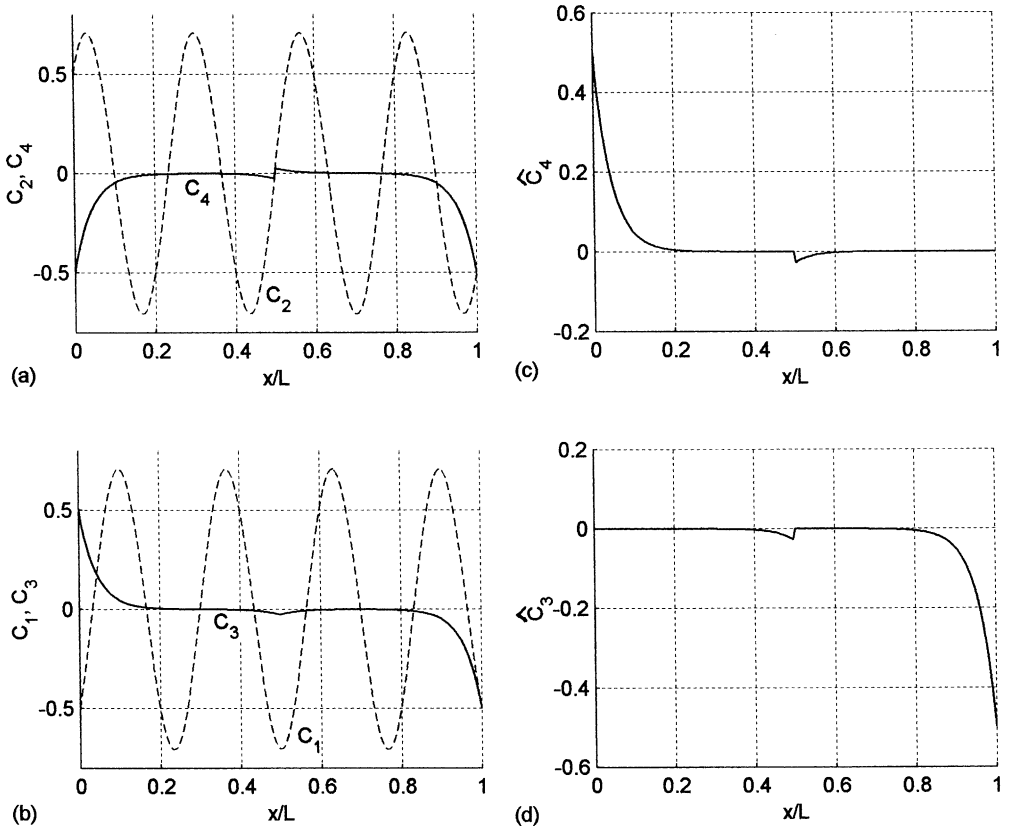

Fig. 6. Central and boundary solutions of the eighth mode shape of the $22'' \times 1'' \times 0.25''$ cantilever with a symmetric center crack obtained using two separate curve-fitting processes for $0 \leqslant x \leqslant L/2$ and $L/2 \leqslant x \leqslant L$: (a) C_2 and C_4, (b) C_1 and C_3, (c) $\widehat{C}_4$, and (d) $\widehat{C}_3$.

After C_i are determined, one can obtain W, W', W'', and W''' for the point at $\bar{x} = 0$ by using the following equations:

$$\begin{aligned} W(0) &= C_1 + C_3 = C_1 + \widehat{C}_3 + \widehat{C}_4 \\ W'(0)/\beta &= C_2 + C_4 = C_2 + \widehat{C}_3 - \widehat{C}_4 \\ W''(0)/\beta^2 &= -C_1 + C_3 = -C_1 + \widehat{C}_3 + \widehat{C}_4 \\ W'''(0)/\beta^3 &= -C_2 + C_4 = -C_2 + \widehat{C}_3 - \widehat{C}_4 \end{aligned} \tag{21}$$

From Eqs. (16) and (21) we know that C_1 represents the central solution of displacement (at $x = x_m$), C_3 represents the boundary solution of displacement caused by boundary constraints, $C_2\beta$ represents the central solution of slope, and $C_4\beta$ represents the boundary solution of slope. Moreover, C_1 and C_3 also separate W'' into central and boundary solutions, and C_2 and C_4 also separate W''' into central and boundary solutions. Furthermore, $\widehat{C}_3$ represents the boundary solution caused by the boundary constraint at $x = L$, and $\widehat{C}_4$ represents the boundary solution caused by the boundary constraint at $x = 0$. In other words, solving the four algebraic equations in Eq. (20) results in answers for the four unknowns $W(0)$, $W'(0)$, $W''(0)$, and $W'''(0)$ with each one being decomposed into two (or three) parts, as shown in Eq. (21).

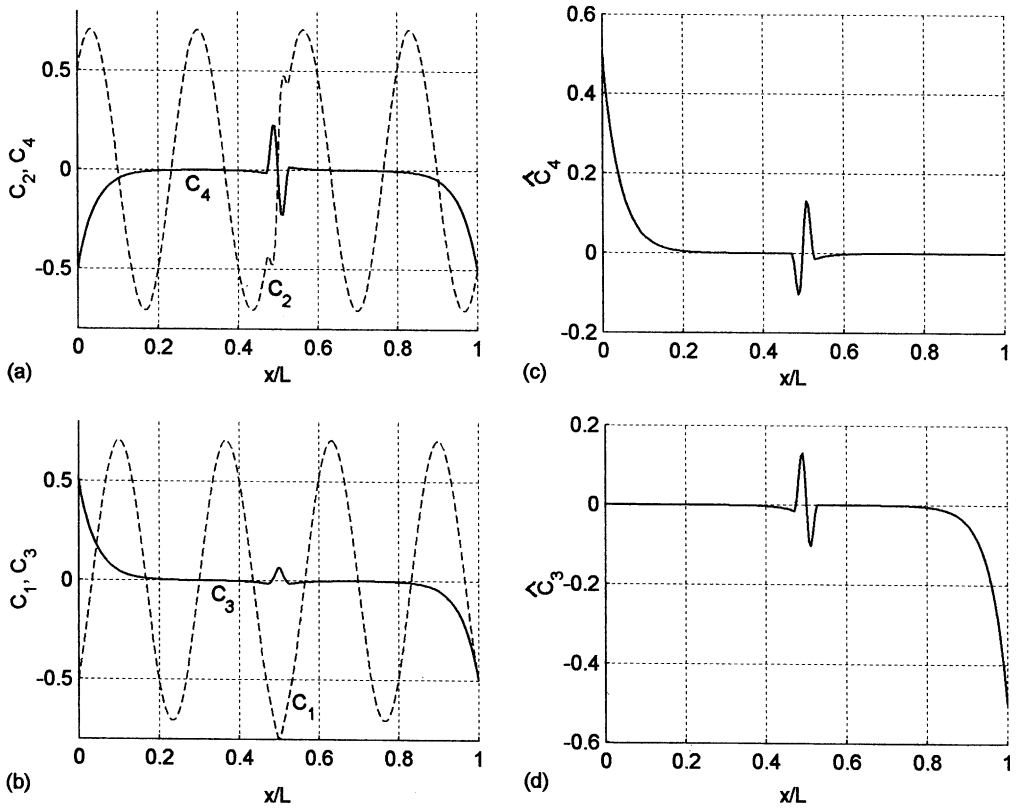

Fig. 7. Central and boundary solutions of the eighth mode shape of the $22'' \times 1'' \times 0.25''$ cantilever with a symmetric center crack obtained using one curve-fitting process for $0 \leqslant x \leqslant L$: (a) C_2 and C_4, (b) C_1 and C_3, (c) $\widehat{C}_4$, and (d) $\widehat{C}_3$.

It follows from Eqs. (21) and (8) that the maximum elastic energy per unit length, Π, is given by

$$\Pi = \tfrac{1}{2}EIW''(0)^2 = \tfrac{1}{2}EI(C_3 - C_1)^2\beta^4 = \tfrac{1}{2}m\Omega^2(C_3 - C_1)^2 \tag{22}$$

Moreover, under steady-state harmonic vibration the maximum kinetic energy per unit length, K, is given by

$$K = \tfrac{1}{2}m(W(0)\Omega)^2 = \tfrac{1}{2}m\Omega^2(C_3 + C_1)^2 \tag{23}$$

Hence it follows from Eqs. (21)–(23) that the difference between these two energy densities is

$$\frac{K - \Pi}{2m\Omega^2} = C_1C_3 = C_1\widehat{C}_3 + C_1\widehat{C}_4 \tag{24}$$

which shows that C_1C_3 is proportional to $K - \Pi$. It follows from Eq. (24) that, if β is large, the boundary solution C_3 should be zero and hence $K - \Pi = 0$ at a point away from boundaries. Because a small damage to a beam introduces a new boundary point to the structure, this is a phenomenon useful for identifying damage locations. Moreover, it can be shown that the integral of K around a boundary point is equal to the integral of Π around the same boundary point (Pai and Young, 2001). In other words, the kinetic energy is locally balanced by the elastic energy, i.e.,

$$\int_{X-\Delta_1}^{X+\Delta_2} (K - \Pi)\,\mathrm{d}x = 0 \tag{25}$$

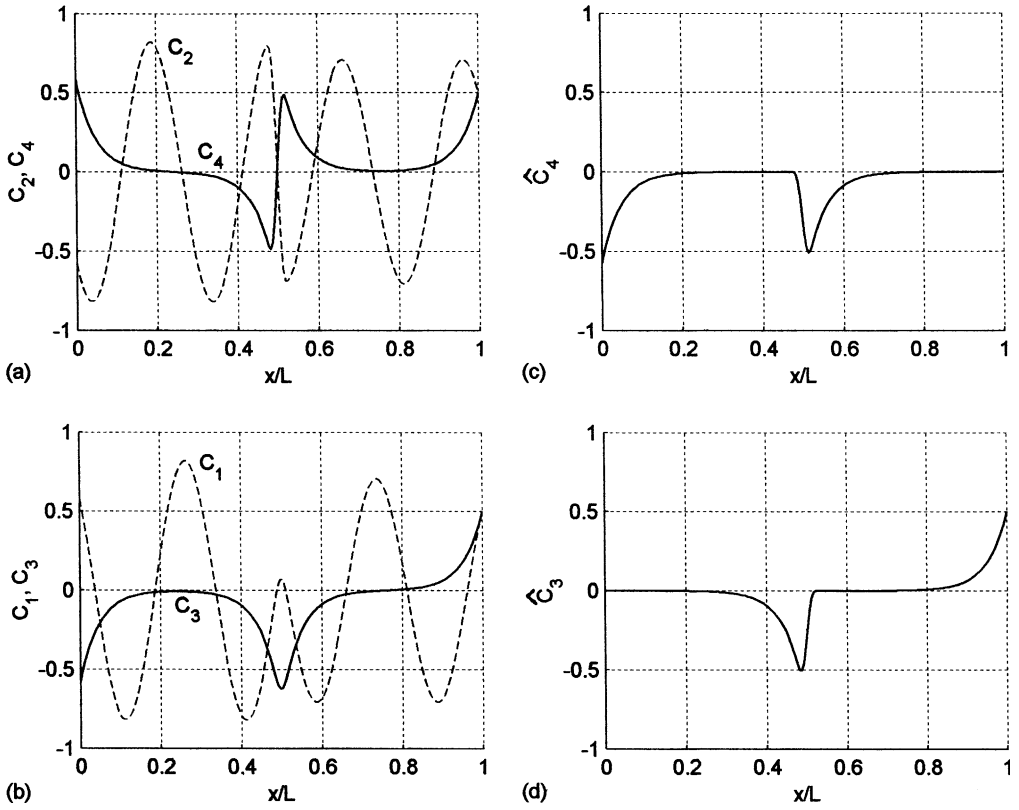

Fig. 8. Central and boundary solutions of the 2100 Hz ODS without crack but an external force at $x = 10.981''$: (a) C_2 and C_4, (b) C_1 and C_3, (c) $\widehat{C}_4$, and (d) $\widehat{C}_3$.

where $x = X$ is the location of a boundary point, and Δ_i can be determined by examining the distribution of $K - \Pi$. If $X = \Delta_1 = \Delta_2 = L/2$ is used, it is always true for any intact or damaged beam. In other words, one can check the energy balance within a local area of a large structure to estimate the degree of damage, without knowing the deformation of the whole structure or the system boundary conditions.

The sectional standard deviation (SSD) and standard deviation (SD) of the fitting process can also be used to monitor the accuracy of curve-fitting and hence reveal damage locations. The SSD is computed as

$$\mathrm{SSD} \equiv \frac{\sqrt{\sum_{i=-N}^{N}[W(\bar{x}_i) - Y(\bar{x}_i)]^2/(2N+1)}}{W_{\max}} \tag{26}$$

where $W_{\max}$ denotes the maximum of W. The overall standard deviation SD is computed after the C_i for every point on the beam are obtained, and it is computed as

$$\mathrm{SD} \equiv \frac{\sqrt{\sum_{m=1}^{M}[W(x_m) - Y(x_m)]^2/M}}{W_{\max}} \tag{27}$$

where M is the total number of points measured along the beam.

The wavenumber β in Eq. (16) needs to be estimated before using the linear sliding-window least-squares method shown in Eqs. (18)–(20). To determine the wavenumber β for a high-frequency deflection shape one

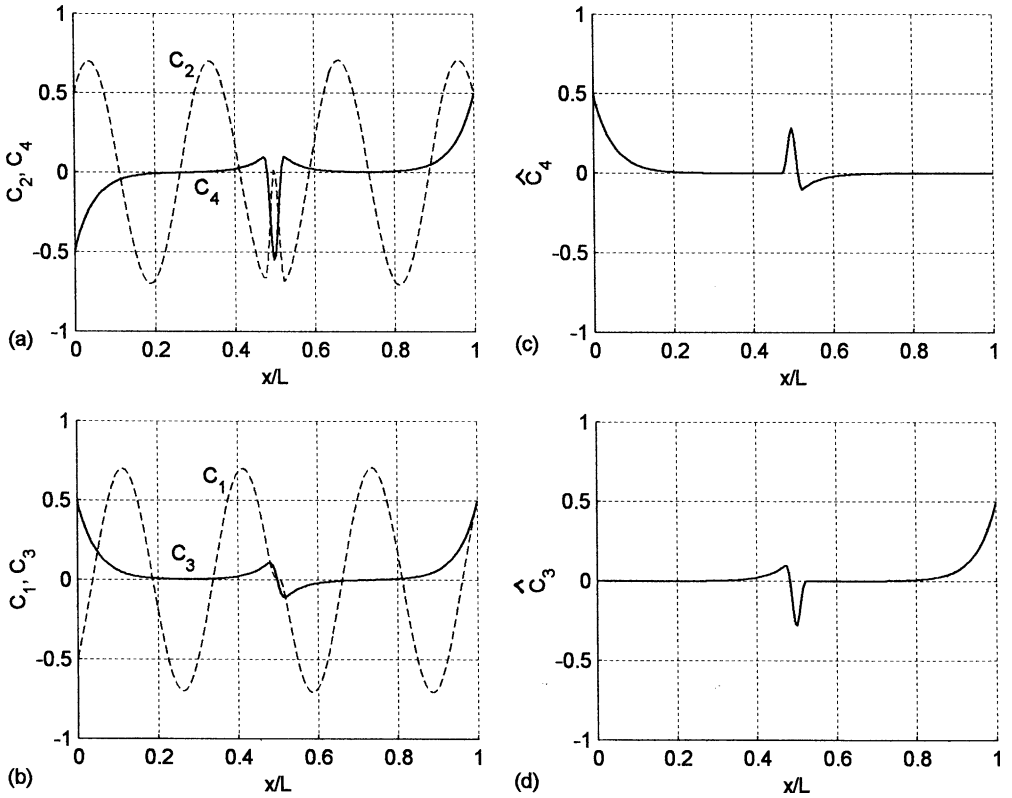

Fig. 9. Central and boundary solutions of the 2100 Hz ODS without crack but an external moment at $x = 10.981''$: (a) C_2 and C_4, (b) C_1 and C_3, (c) $\widehat{C}_4$, and (d) $\widehat{C}_3$.

can plot the experimental ODS, pick up a length $\tilde{L}$ covering n times of the wavelength λ, and obtain $\beta = 2\pi n/\tilde{L}$. For a low-frequency deflection shape, it is difficult to obtain an accurate estimation of β from the ODS using this approach, but one can use a non-linear curve-fitting method to improve the estimation of β (Pai and Jin, 2000). Numerical and experimental results show that the proposed method for extracting boundary solutions requires an accurate estimation of β only if it is a high-frequency ODS. However, if the estimated β is not accurate, the sectional standard deviation and boundary solutions will show periodic change. Hence, it is easy to know whether the estimated β is correct, and, if necessary, one can revise the estimation and rerun the signal processing.

5. Numerical simulations

Next we perform numerical simulations of dynamic characteristics, ODSs, damage detection, and identification of boundary conditions of beams.

5.1. Dynamic characteristics

We consider the beam shown in Fig. 2(a) with $L = 22''$, $b = 1''$, $h = 0.25''$, $a + c/2 = L/2$, $c = 0.039''$, $e = 0.2h$, Young's modulus $E = 10.6 \times 10^6$ psi, Poisson's ratio $v = 0.33$, and a mass density $\rho = 5.37$ slug/ft^3.

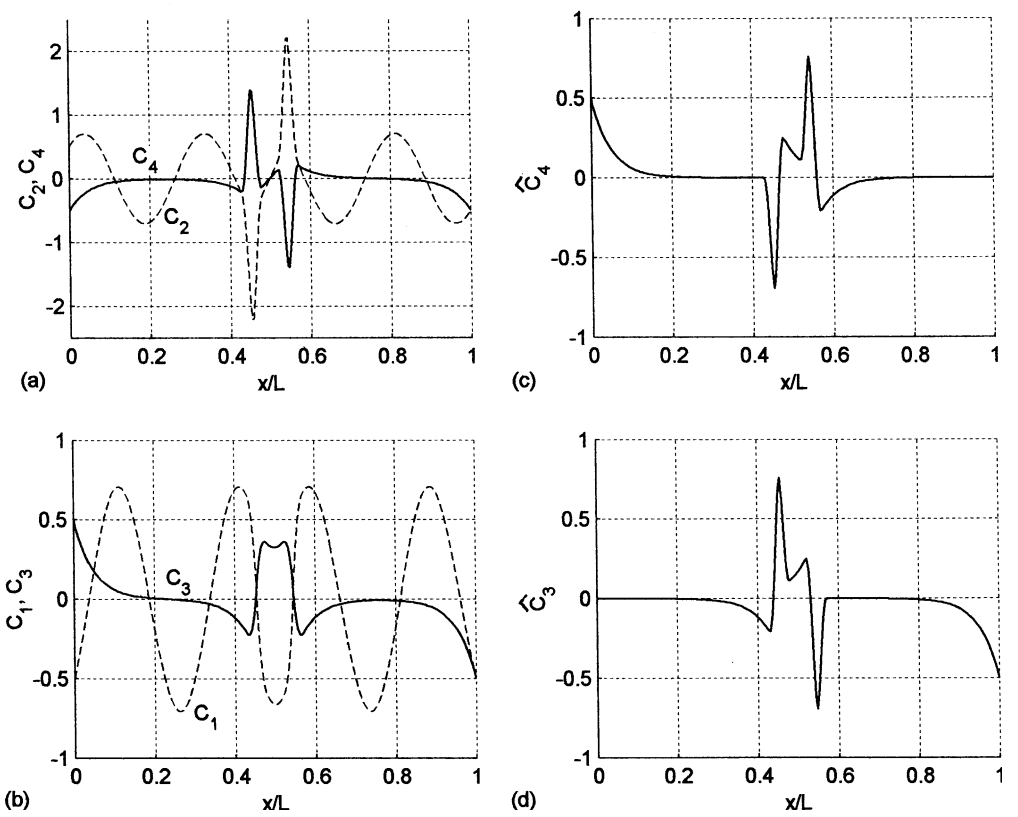

Fig. 10. Central and boundary solutions of the 2100 Hz ODS without crack but an external moment $-M$ at $x = 10''$ and an external moment M at $x = 12''$: (a) C_2 and C_4, (b) C_1 and C_3, (c) $\widehat{C}_4$, and (d) $\widehat{C}_3$.

Moreover, we consider clamped-free boundary conditions, i.e., $\tau_1 = \tau_2 = 0$. Using the spectral element method shown in Section 3.2 we obtain the first 10 natural frequencies to be 16.859, 105.18, 296.22, 577.25, 959.57, 1425.6, 2002.1, 2651.1, 3423.7, 4253.8 Hz. Fig. 3 shows the eighth ϕ, ϕ', ϕ'', and ϕ''', where there is no data point representing the slotted segment because the slot width c is so small. We note that ϕ' and ϕ''' are discontinuous at $x = L/2$, but ϕ and ϕ'' are continuous; however, the discontinuity of ϕ''' is small. The discontinuity of ϕ' is mainly due to the action of the two concentrated moments at $x = a$ and $x = a + c$, as shown by Eq. (4). The discontinuity of ϕ''' is due to the action of the distributed load between at $x = a$ and $x = a + c$ caused by the inertia force, as shown by Eq. (4). In other words, if the crack width c is very small, we have

$$w(a^-) = w(a + c^+), \qquad w'(a^-) \neq w'(a + c^+), \qquad w''(a^-) = w''(a + c^+), \qquad w'''(a^-) \neq w'''(a + c^+) \tag{28}$$

Hence, the beam in Fig. 2(a) can be modeled as that in Fig. 2(b) using two beam elements and two springs to account for the slot with

$$\hat{\tau}_1 = \frac{-cEI_1 W^{iv}(a^+)}{W(a^+)} = \frac{-cEI_1\beta^4 W(a^+)}{W(a^+)} = -cm_1\Omega^2, \qquad \hat{\tau}_2 = \frac{EI_1 W''(a^+)}{W'(a + c^+) - W'(a^-)} = \frac{EI_1}{c} \tag{29}$$

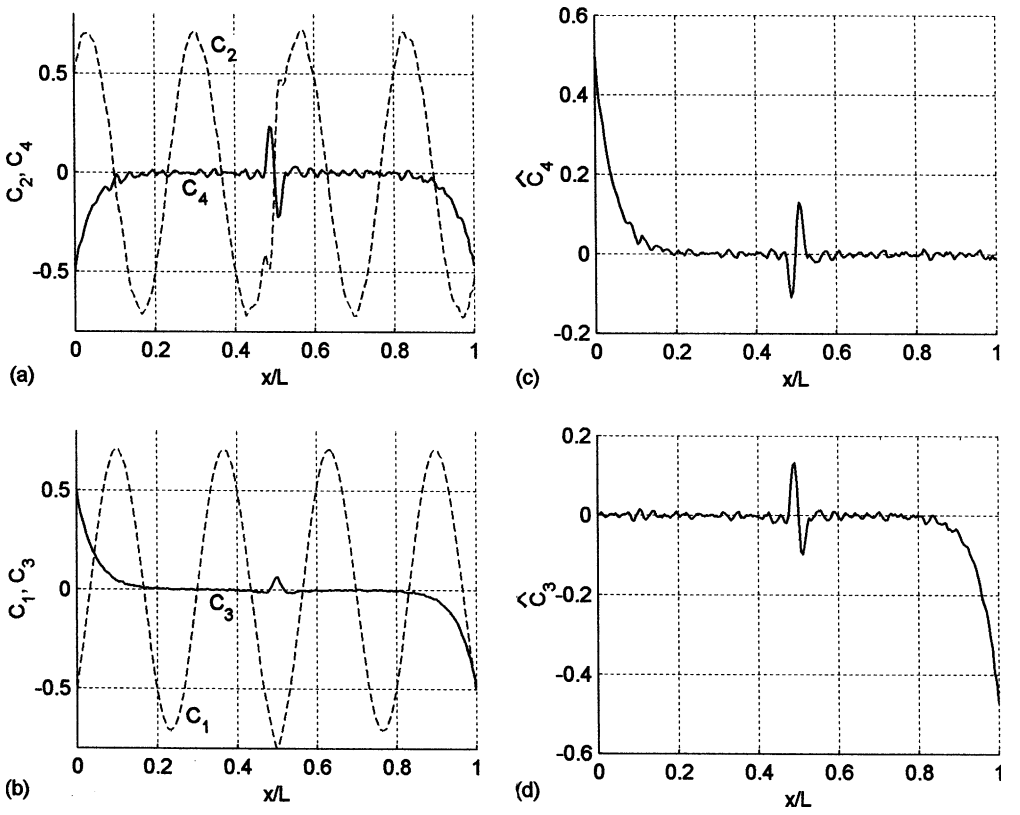

Fig. 11. Central and boundary solutions and damage detection curves of the eighth mode shape with a symmetric center crack and 0.05% random noise added: (a) C_2 and C_4, (b) C_1 and C_3, (c) $\widehat{C}_4$, (d) $\widehat{C}_3$, (e) W (dots), W'/β ($= C_2 + C_4$, thin line), W''/β^2 ($= C_3 - C_1$, broken line), and W'''/β^3 ($= C_4 - C_2$, thick line), (f) SSD, (g) C_4, and (h) C_1C_3.

Here $\hat{\tau}_1$ is the equivalent linear spring constant accounting for the inertia force of the slotted segment, $m_1 \equiv m(h-2e)/h$ is the mass per unit length of the slotted segment, and $\hat{\tau}_2$ is the equivalent torsional spring constant accounting for the bending stiffness of the slotted segment. Using this two-element model we obtain the first ten natural frequencies to be 16.905, 105.18, 296.27, 577.25, 962.98, 1425.6, 2009.1, 2651.1, 3435.8, 4253.8 Hz. Apparently, the model shown in Fig. 2(b) represents the damaged beam well because the ω_i, $i = 2, 4, 6, 8, 10$ are exact, and the errors of ω_i, $i = 1, 3, 5, 7, 9$ are less than 0.4%, which is because the two concentrated forces at $x = a$ and $x = a + c$ (see Eq. (4)) are not accounted for in the model shown in Fig. 2(b) but they are non-zero for odd modes around $x = L/2$.

Although the stress concentration around a sudden change of cross section increases the bending curvature and makes damage effects more significant, it is difficult to estimate the stress concentration because it is a complex function of size, geometry, and other factors. Hence, the stress concentration effect is neglected in the numerical simulations.

Fig. 4 compares the seventh and eighth mode shapes, ϕ_7 and ϕ_8, with the 2100 Hz ODS with an excitation force applied at $x = a(= (L-c)/2)$. Although $\omega_7 = 2002.1$ Hz and $\omega_8 = 2651.1$ Hz, the 2100 Hz ODS is closer to ϕ_8 because the excitation is very close to the node of ϕ_7 at $x = L/2$. However, the two peaks of the ODS around $x = L/2$ with different magnitudes indicate that ϕ_7 has non-trivial contribution because Ω is close to ω_7. Moreover, if the excitation is a 2100 Hz moment at $x = a$, the ODS will be

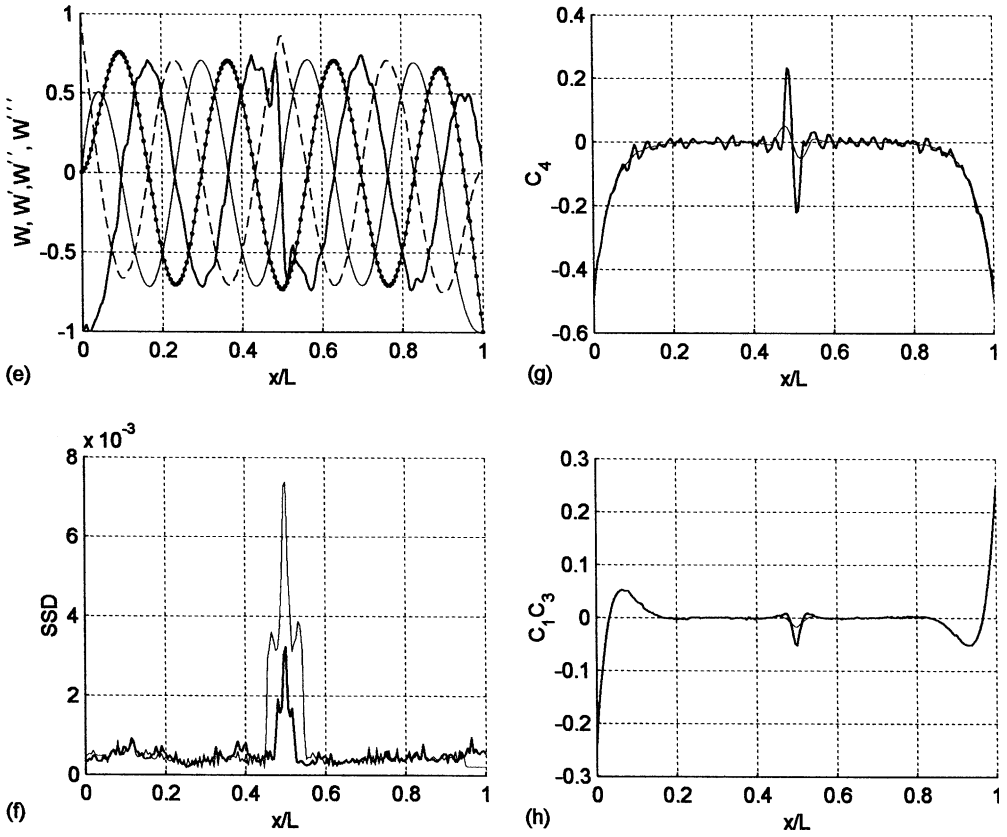

Fig. 11 (*continued*)

dominated by ϕ_7 because $\phi_7'(a) \neq 0$ and Ω is close to ω_7. In other words, the shape of an ODS depends on the frequency, location, and type of excitation.

If there is no damage (i.e., $e = 0$) and the beam is uniform, Fig. 5(a) shows the W, W', W'', and W''' with a 2100 Hz excitation force at $x = a$, and Fig. 5(b) shows the ODS with a 2100 Hz excitation moment at $x = a$. The concentrated external force causes the cusp of W'' and the discontinuity of W''', and the concentrated external moment causes the cusp of W' and the discontinuity of W''. The big discontinuity of W''' is due to the large transverse force required to excite the ODS that is similar to ϕ_8 but the excitation frequency Ω is away from ω_8. The small discontinuity of W'' is due to the small moment required to excite the ODS that is similar to ϕ_7 and the excitation frequency Ω is close to ω_7. If W is obtained using Eq. (9) with 100 mode shapes, the cusp on W'' and the discontinuity on W''' in Fig. 5(a) disappear because ϕ_i, ϕ_i', ϕ_i'', and ϕ_i''' are continuous functions. Hence, Eqs. (7) and (9) are not really exact. Fig. 3 shows that a crack causes the discontinuity on ϕ' (or W') and ϕ''' (or W'''). Because the influences of different external loads and damage on ODSs have different characters, it should be possible to identify them separately using ODSs and their derivatives.

5.2. Damage detection

Fig. 6 shows the results obtained using the BED method shown in Section 4 to process the eighth mode shape with $a + c/2 = L/2$, $c = 0.039''$, and $2e/h = 0.4$. Two curve-fitting processes are performed for

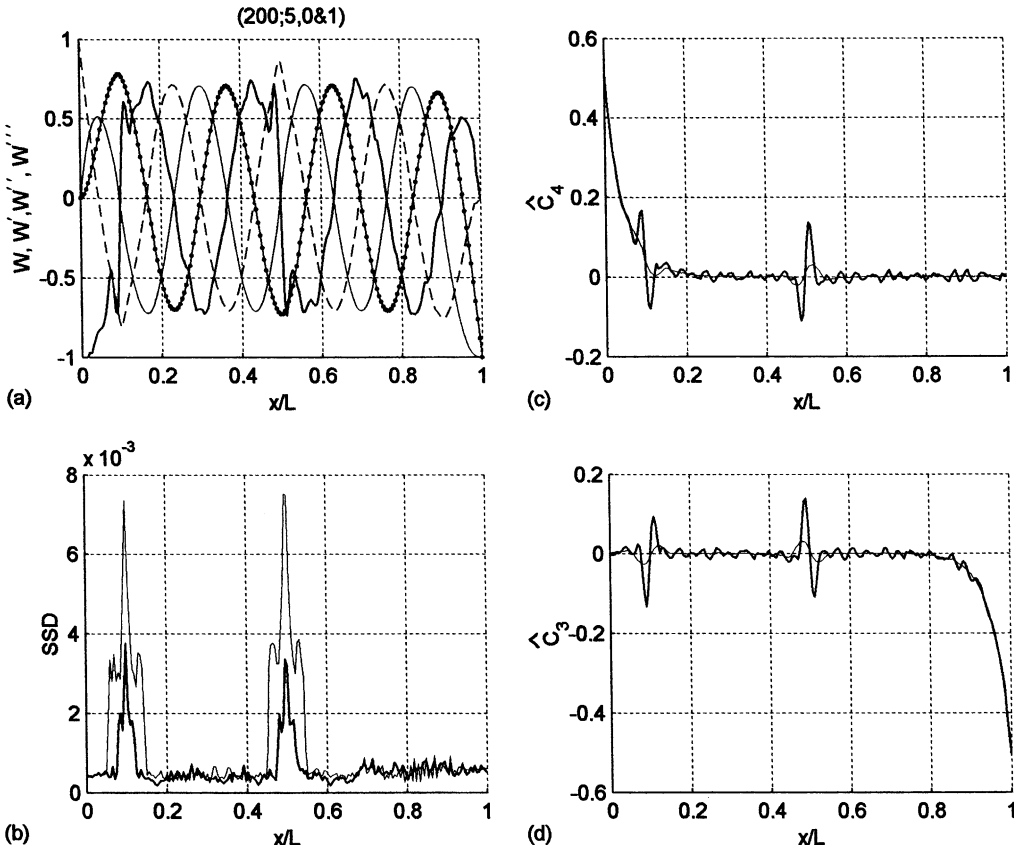

Fig. 12. Damage detection curves of the eighth mode shape with two cracks having $c = 0.039''$ and $2e = 0.4h$ at $x = 0.1L$ and $x = 0.5L$ and 0.05% random noise added: (a) W (dots), W'/β (thin line), W''/β^2 (broken line), and W'''/β^3 (thick line), (b) SSD, (c) $\widehat{C}_4$, and (d) $\widehat{C}_3$.

Table 1
Different boundary conditions of high-frequency ODSs around $x = 0$

	General ($\theta_1 + \theta_2 = 90°$)	Clamped ($\theta_1 = \theta_2 = 45°$)	Hinged ($\theta_1 = 90°$, $\theta_2 = 0°$)	Sliding ($\theta_1 = 0°$, $\theta_2 = 90°$)	Free ($\theta_1 = \theta_2 = 45°$)
C_1	$-A\cos(\beta x + \theta_1)$	$-A\cos(\beta x + 45°)$	$A\sin(\beta x)$	$-A\cos(\beta x)$	$-A\cos(\beta x + 45°)$
C_2	$A\cos(\beta x - \theta_2)$	$A\cos(\beta x - 45°)$	$A\cos(\beta x)$	$A\sin(\beta x)$	$A\cos(\beta x - 45°)$
C_3	$\tilde{A}\,e^{-\beta x}$	$\frac{A}{\sqrt{2}}e^{-\beta x}$	0	0	$-\frac{A}{\sqrt{2}}e^{-\beta x}$
C_4	$-\tilde{A}\,e^{-\beta x}$	$-\frac{A}{\sqrt{2}}e^{-\beta x}$	0	0	$\frac{A}{\sqrt{2}}e^{-\beta x}$
$\widehat{C}_3\left(=\frac{C_3+C_4}{2}\right)$	0	0	0	0	0
$\widehat{C}_4\left(=\frac{C_3-C_4}{2}\right)$	$\tilde{A}\,e^{-\beta x}$	$\frac{A}{\sqrt{2}}e^{-\beta x}$	0	0	$-\frac{A}{\sqrt{2}}e^{-\beta x}$
$W(=C_1+C_3)_{x=0}$	$\tilde{A} - A\cos\theta_1$	0	0	$-A$	$-\sqrt{2}A$
$W'/\beta(=C_2+C_4)_{x=0}$	$A\cos\theta_2 - \tilde{A}$	0	A	0	$\sqrt{2}A$
$W''/\beta^2(=C_3-C_1)_{x=0}$	$\tilde{A} + A\cos\theta_1$	$\sqrt{2}A$	0	A	0
$W'''/\beta^3(=C_4-C_2)_{x=0}$	$-A\cos\theta_2 - \tilde{A}$	$-\sqrt{2}A$	$-A$	0	0

$0 \leqslant x \leqslant a$ and $a + c \leqslant x \leqslant L$, respectively. The maximum SSD is less than 10^{-13}. The results show that the central solutions C_1 and C_2 are smooth harmonic functions, the boundary solution C_3 is continuous but has

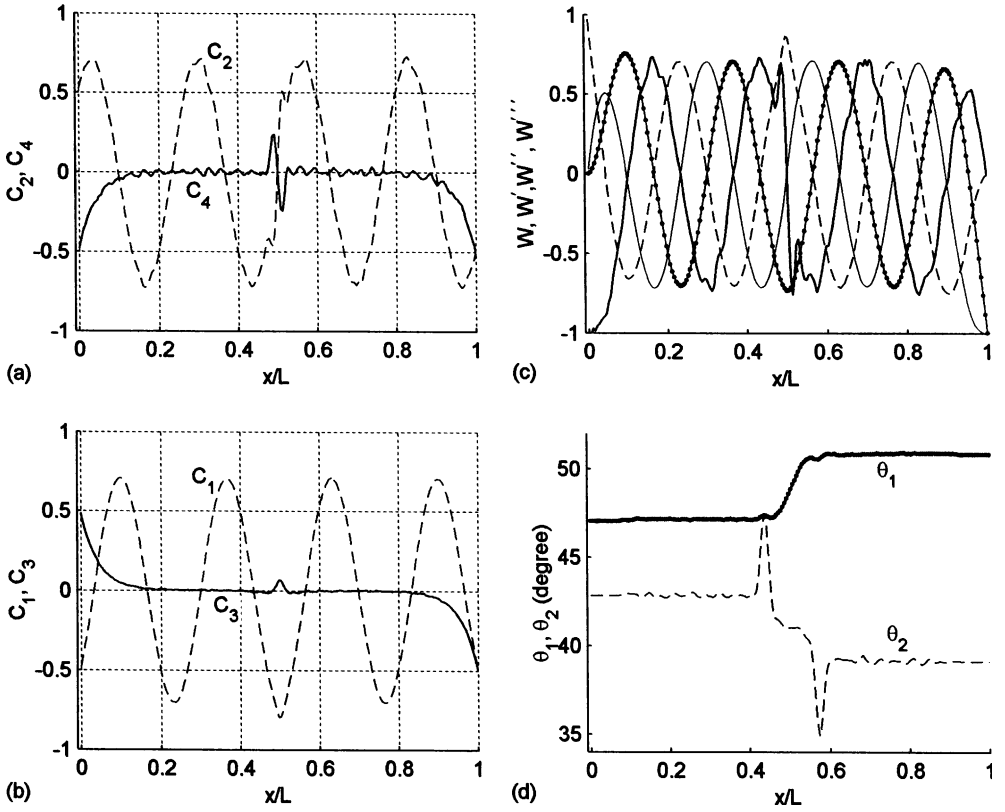

Fig. 13. Boundary condition detection curves of the eighth mode shape with one crack having $c = 0.01''$ and $2e = 0.4h$ at $x = 0$ and one crack having $c = 0.039''$ and $2e = 0.4h$ at $x = 0.5L$ and 0.05% random noise added: (a) C_2 and C_4, (b) C_1 and C_3, (c) W (dots), W'/β (thin line), W''/β^2 (broken line), and W'''/β^3 (thick line), and (d) θ_1 and θ_2.

a cusp at the location of damage, the boundary solutions C_4, $\widehat{C}_3$ and $\widehat{C}_4$ are discontinuous at the damage location. Because C_4 is discontinuous, it follows from Eq. (21) that W' and W''' are discontinuous. We note that the right-end boundary solution $\widehat{C}_3$ and the left-end boundary solution $\widehat{C}_4$ are well separated. Because $e = 0.2h$, the damage is considered to be big, but the damage indicators shown in Fig. 6 are not very significant, especially if noise exists. If only one curve-fitting process is performed for the whole beam $0 \leqslant x \leqslant L$, Fig. 7 shows the results. We note that all C_i and $\widehat{C}_j$ are continuous because the four continuous functions shown in Eq. (16) are used in the curve-fitting. However, because W' and W''' are discontinuous, the use of continuous functions to fit such a discontinuous function results in Gibbs' phenomenon. We note that the significant sign changes of C_4, $\widehat{C}_3$ and $\widehat{C}_4$ and the peak of C_3 at the damage location in Fig. 7 are caused by Gibbs' phenomenon. Gibbs' phenomenon also makes C_1 and C_2 non-smooth. Hence, Gibbs' phenomenon actually makes the identification of damage easier.

Fig. 8 shows the results obtained by processing the 2100 Hz ODS shown in Fig. 5(a). We note that the styles of boundary and central solutions are very different from those in Fig. 7 because the discontinuity is due to a shear force. Fig. 9 shows the results obtained by processing the 2100 Hz ODS shown in Fig. 5(b). We note that the styles of boundary and central solutions are very different from those in Figs. 7 and 8 because the discontinuity is due to a bending moment. Fig. 10 shows the results obtained by processing the 2100 Hz ODS under a moment $-M$ at $x = 10''$ and a moment M at $x = 12''$. The loading condition is similar to that caused by a $2''$ long PZT patch. We note that the styles of boundary and central solutions are more

complex than those in Figs. 7–9 because the discontinuities are due to two bending moments. Hence, it is possible to distinguish boundary solutions due to damage, actual boundaries, external forces, and external bending moments from each other.

Because ODSs obtained using a scanning laser vibrometer always contain noise due to spectral noise and other factors, we also consider ODSs with noise. Fig. 11 shows the curve-fitted results obtained by processing the eighth mode shape with $a + c/2 = L/2$, $c = 0.039''$, $2e/h = 0.4$ and 0.05% uniformly distributed random noise added. $N = 5$ (see Eq. (18)) and $\Delta x = L/200$ (i.e., the space between two adjacent sample

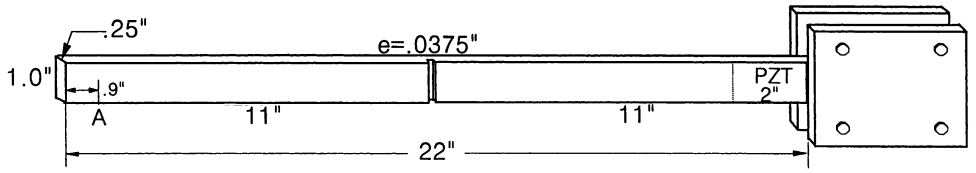

Fig. 14. A free-clamped beam with an asymmetric center crack.

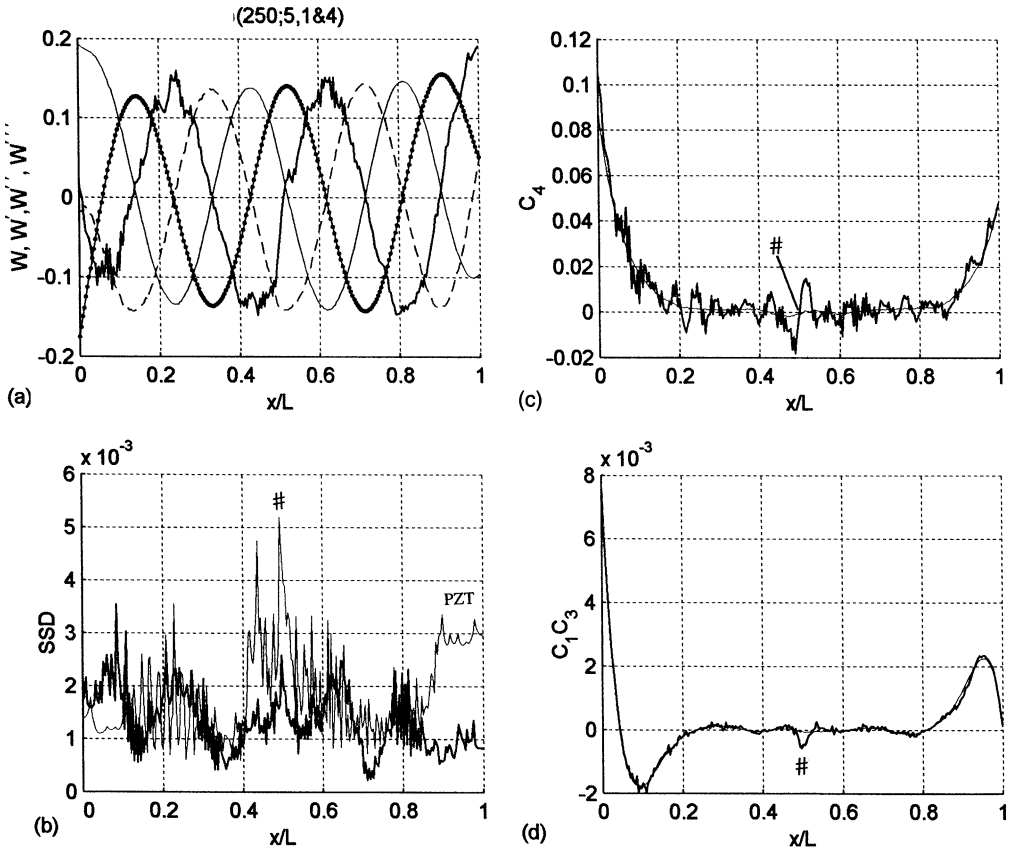

Fig. 15. Damage detection curves of the 1295 Hz ODS of the free-clamped $22'' \times 1'' \times 0.25''$ aluminum beam having a crack with $c = 0.039''$ and $e = 0.15h$ at $x = 11''$: (a) W (dots), W'/β (thin line), W''/β^2 (broken line), and W'''/β^3 (thick line), (b) SSD, (c) C_4, and (d) C_1C_3.

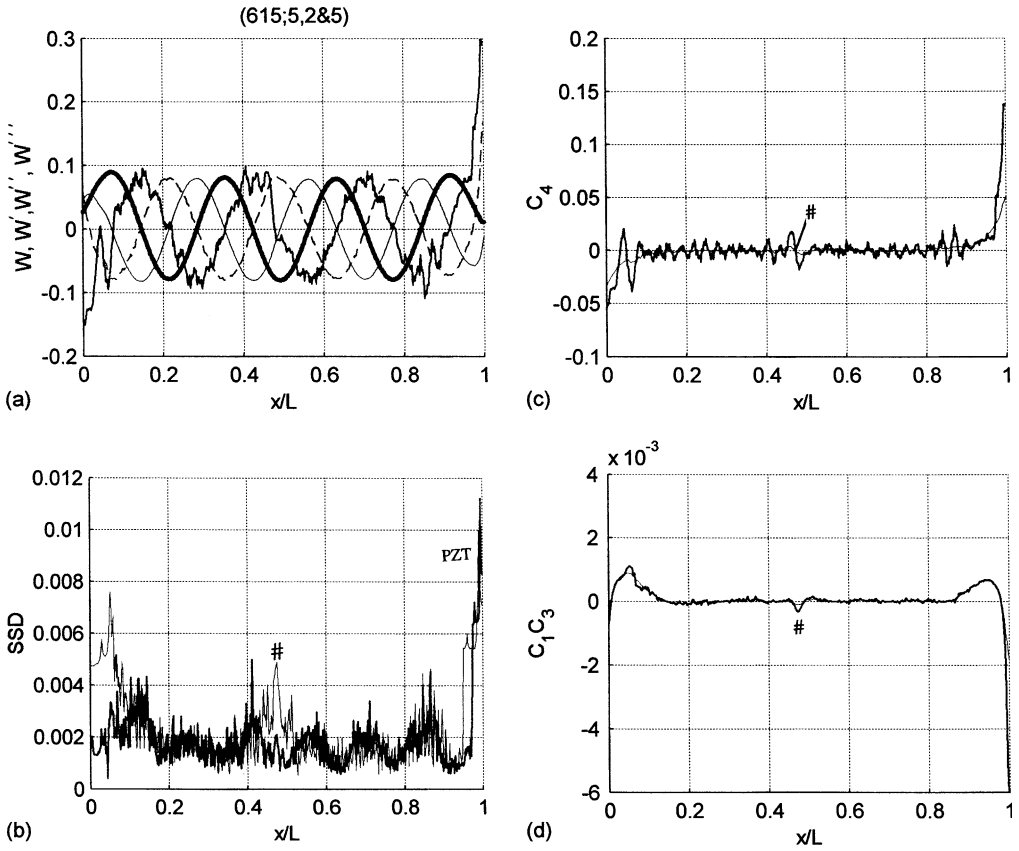

Fig. 16. Damage detection curves of the 2612.5 Hz ODS of the clamped (without tape)-clamped $21.1'' \times 1'' \times 0.25''$ aluminum beam having a crack with $c = 0.039''$ and $e = 0.15h$ at $x = 10.1''$: (a) W (dots), W'/β (thin line), W''/β^2 (broken line), and W'''/β^3 (thick line), (b) SSD, (c) C_4, and (d) C_1C_3.

points) are used. The C_3, C_4, $\widehat{C}_3$ and $\widehat{C}_4$ still clearly indicate the damage location, but C_4, $\widehat{C}_3$ and $\widehat{C}_4$ are rough. The SSD and C_1C_3 also clearly indicate the damage location. The thin lines in Fig. 11(f)–(h) are obtained using $N = 5$ and $\Delta x = 2L/200$, i.e., doubled the sliding-window length $2N\Delta x$.

Fig. 12 shows the curve-fitted results obtained by processing the eighth mode shape with two cracks having $c = 0.039''$ and $2e = 0.4h$ at $x = 0.1L$ and $x = 0.5L$. Although the left crack is within the boundary zone, the sign change of the right-end boundary solution $\widehat{C}_3$ clearly indicate the crack location.

We note that, if Eq. (16) is used to fit the whole ODS (or a selected section) without using a sliding window, one can only obtain one value for each of the four coefficients c_i. Then, the fitted ODS is an average representation of the actual ODS, and no local variation can be revealed. If a cubic polynomial is used in the curve-fitting with the use of a sliding window, one can show that

$$\begin{aligned} &W(\bar{x}) = D_1 + D_2\bar{x} + D_3\bar{x}^2 + D_4\bar{x}^3 \\ &W(0) = D_1, \qquad W'(0) = D_2, \qquad W''(0) = 2D_3, \qquad W'''(0) = 6D_4 \end{aligned} \tag{30}$$

We note that boundary solutions cannot be separated from the central solutions. Moreover, the D_i have values of different orders and are difficult to be compared in one figure.

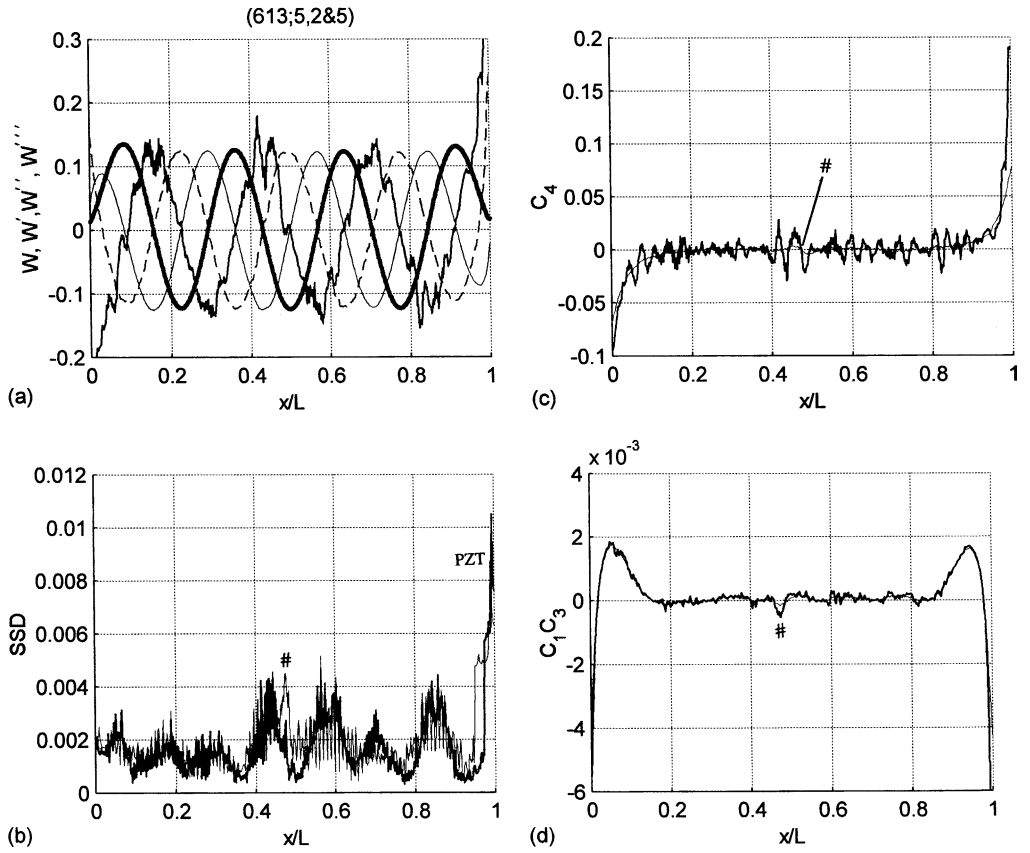

Fig. 17. Damage detection curves of the 2612.5 Hz ODS of the clamped (with tape)-clamped $21.1'' \times 1'' \times 0.25''$ aluminum beam having a crack with $c = 0.039''$ and $e = 0.15h$ at $x = 10.1''$: (a) W (dots), W'/β (thin line), W''/β^2 (broken line), and W'''/β^3 (thick line), (b) SSD, (c) C_4, and (d) C_1C_3.

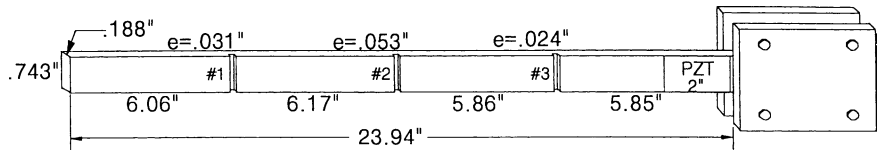

Fig. 18. A free-clamped aluminum beam with three cracks.

5.3. Identification of boundary conditions

For one general and four perfect boundary conditions, Table 1 shows boundary and central solutions of high-frequency ODSs around the boundary at $x = 0$. We note that, for any boundary condition around $x = 0$, $C_1 = -A\cos(\beta x + \theta_1)$, $C_2 = A\cos(\beta x - \theta_2)$, and $\theta_1 + \theta_2 = 90°$. For the four perfect boundary conditions, θ_1 and θ_2 are equal to 0°, 45° or 90°, as shown in Table 1. Because a general boundary point can be connected to a linear spring, a torsional spring, a translational mass, a rotational mass, a linear damper, a

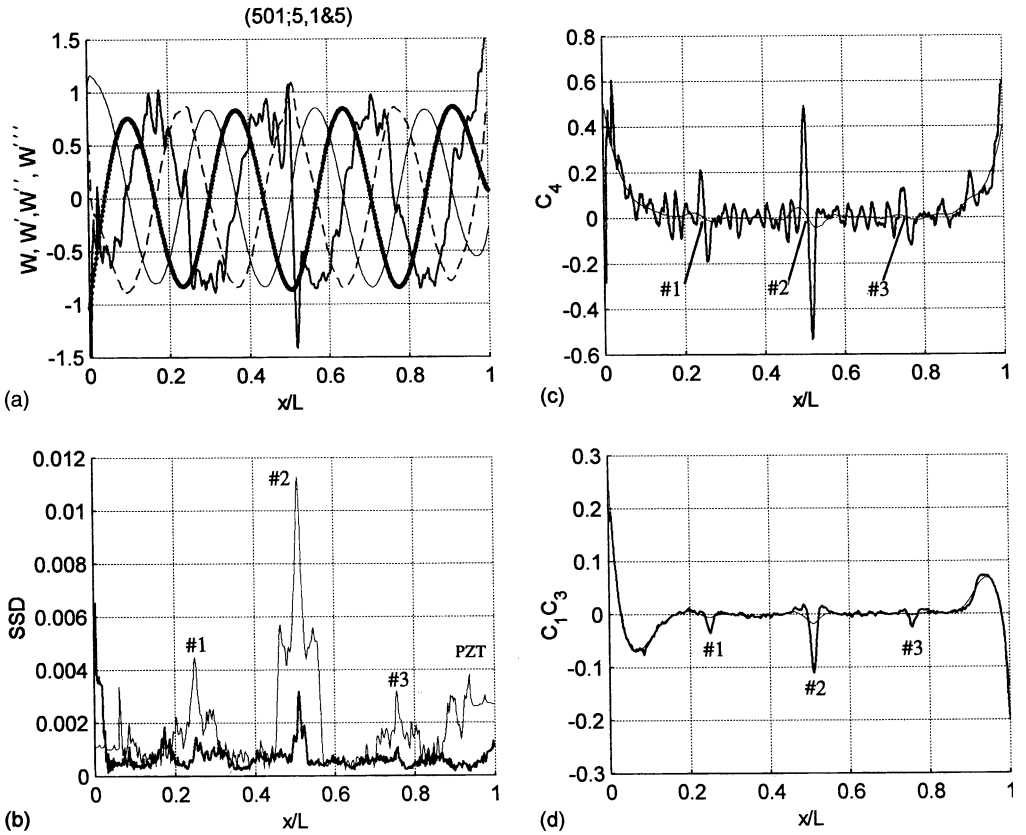

Fig. 19. Damage detection curves of the 1556.25 Hz ODS of the free-clamped $23.94'' \times 0.743'' \times 0.188''$ beam with three cracks using $N = 5$ and $\Delta x = 2L/501$: (a) W (dots), W'/β (thin line), W''/β^2 (broken line), and W'''/β^3 (thick line), (b) SSD, (c) C_4, and (d) C_1C_3.

torsional damper, an external force, and/or an external moment, the amplitude of boundary solutions, $\tilde{A}$, may not be equal to $A/\sqrt{2}$ and θ_1 and θ_2 may not be equal to 0°, 45° or 90° although $\theta_1 + \theta_2 = 90°$.

Fig. 13 shows the curve-fitted results obtained by processing the eighth mode shape with a crack within $0 \leqslant x \leqslant 0.01''$ and $2e/h = 0.4$ and another crack having $c = 0.039''$, $2e/h = 0.4$, $a + c/2 = L/2$ and 0.05% noise added. We note that, although the crack depth $2e$ is 40% of the thickness, the boundary and central solutions do not deviate much from those of a perfectly clamped condition shown in Table 1, except that W' has a small value at $x = 0$. Hence, it is difficult to identify actual boundary conditions using boundary or central solutions. However, $\theta_1 = 47.08° > 45°$ and $\theta_2 = 42.84° < 45°$ clearly indicate that the boundary is not perfectly clamped, which is due to the crack at $x = 0$. Moreover, the sudden change of θ_1 and θ_2 around $x = L/2$ also indicate the second crack. Because C_1 and C_2 are smoother than C_3, C_4, $\widehat{C}_3$, and $\widehat{C}_4$ (see Fig. 11), the extraction of θ_1 and θ_2 from C_1 and C_2 are not sensitive to the presence of noise. For example, when 0.5% random noise is added to the mode shape, the distributions of θ_1 and θ_2 are still able to reveal the non-perfect boundary at $x = 0$ and the crack at $x = L/2$ but all other boundary and central solutions are too shaky to reveal the damage. If the boundary point at $x = 0$ is known and can be reached for measurement, one can use θ_i to check whether there is any damage. If the boundary point at $x = 0$ is unknown and/or cannot be reached for measurement, one can also use θ_i to estimate the location of the left end.

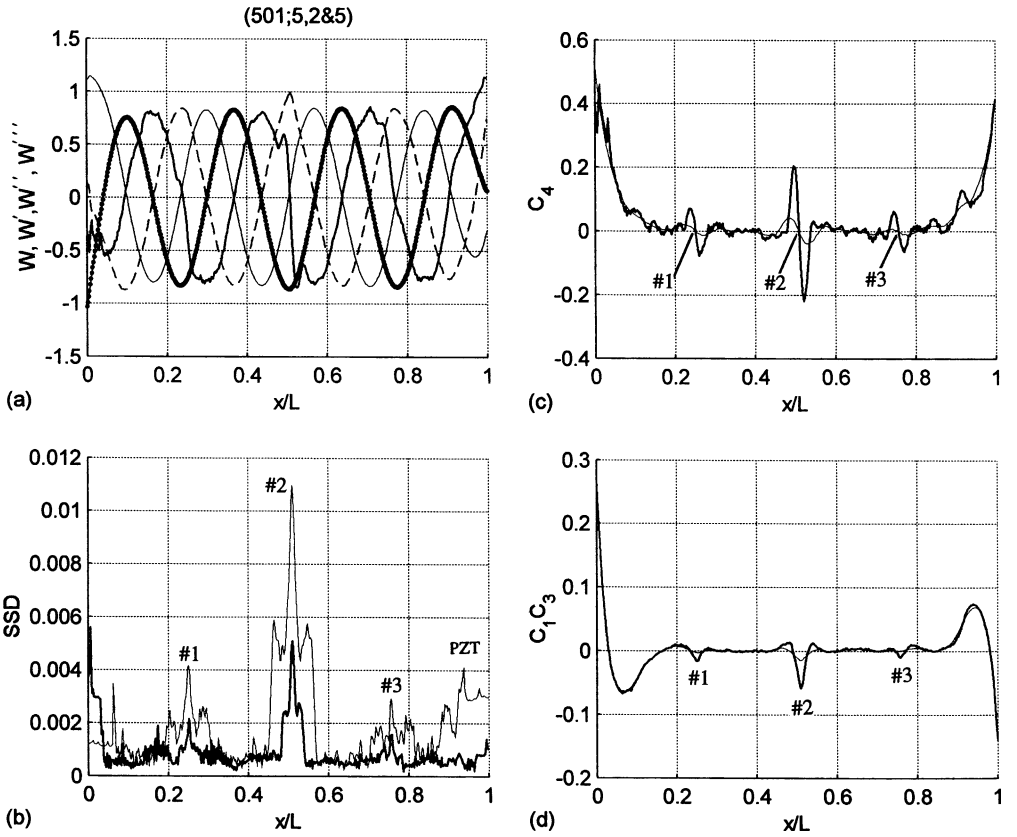

Fig. 20. Damage detection curves of the 1556.25 Hz ODS of the free-clamped $23.94'' \times 0.743'' \times 0.188''$ beam with three cracks using $N = 5$ and $\Delta x = 3L/501$: (a) W (dots), W'/β (thin line), W''/β^2 (broken line), and W'''/β^3 (thick line), (b) SSD, (c) C_4, (d) C_1C_3, (e) C_2 and C_4, (f) C_1 and C_3, (g) $\widehat{C}_4$, and (h) $\widehat{C}_3$.

6. Experimental results

Fig. 14 shows a free-clamped $22'' \times 1'' \times 0.25''$ aluminum beam with a center crack having a crack width $c = 0.039''$ and a crack depth $e = 0.0375''(= 0.15h)$. Fig. 15 shows the results obtained using the BED method with $N = 5$ (see Eq. (18)) and $\Delta x = 2L/250$ (i.e., the space between two adjacent sample points) to process the 1295 Hz ODS, which was excited by the PZT patch shown in Fig. 14 and was measured at 250 ($= M$, see Eq. (27)) points using the scanning laser vibrometer from the backside of the beam. The thin lines in Fig. 15(b)–(d) are obtained using $N = 5$ and $\Delta x = 5L/250$. Fig. 15(a) shows that it is difficult to find the crack by examining the ODS W ($= C_1 + C_3$, dots), W'/β ($= C_2 + C_4$, thin line), W''/β^2 ($= C_3 - C_1$, broken line), or W'''/β^3 ($= C_4 - C_2$, thick line). On the other hand, the peak of SSD, the dimple of C_1C_3, and the sign change of C_4 at $x = 0.5L$ clearly indicate the crack location. The peak of SSD around $x = L$ is due to the bending moment from the PZT patch. The peak of SSD around $x = 0.45L$ when $\Delta x = 5L/250$ is caused by coupling with the peak at $x = 0.5L$ (see the side-lobes in Fig. 11(f)) and there is no damage at $x = 0.45L$ because it becomes relatively small when Δx is reduced to $2L/250$. Because the first measurement point is actually about $0.1''$ to the right of the free end, requiring $\theta_1 = 45°$ and matching the theoretical C_1 function of a free end shown in Table 1 with the curve-fitted C_1 curve indicates that the free end is at $x = -0.1''$, as it should be.

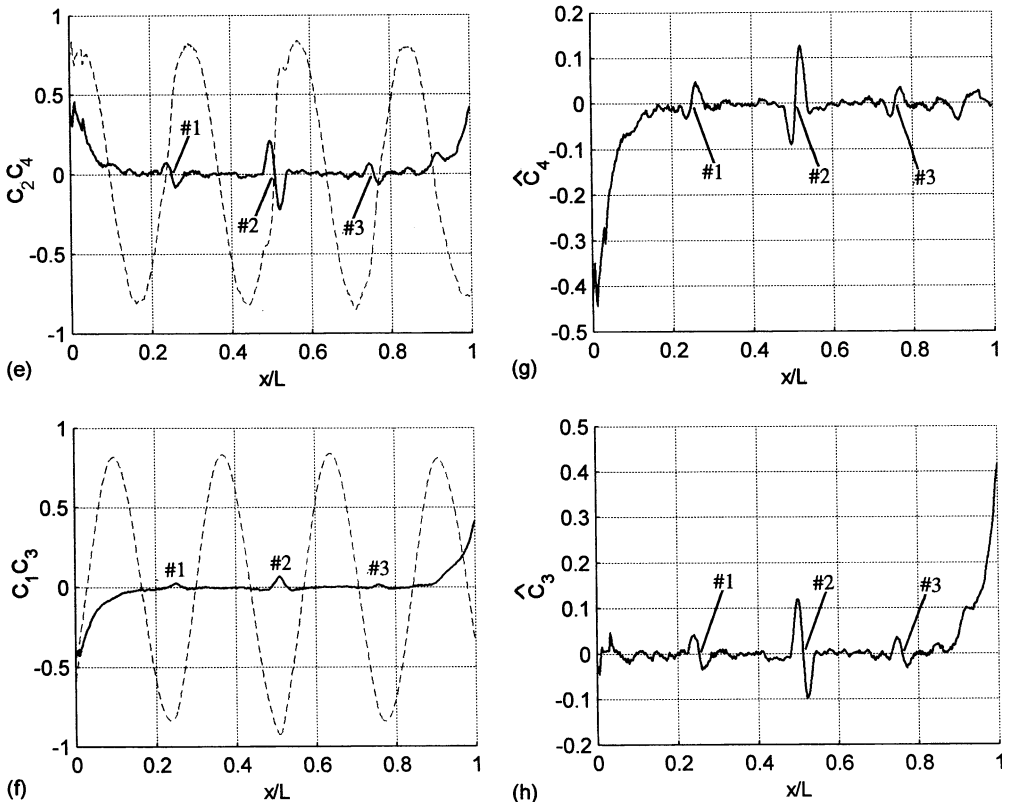

Fig. 20 (*continued*)

Then a $0.9''$ section of the left end was clamped using two steel plates in a way similar to the right clamped end. Fig. 16 shows the curve-fitted results obtained by processing the 2612.5 Hz ODS using $N = 5$ and $\Delta x = 3L/615$. The thin lines in Fig. 16(b)–(d) are obtained using $N = 5$ and $\Delta x = 6L/615$. The frequency was picked up from the seventh peak on the averaged FRF obtained using a 0–20 kHz periodic chirp excitation. Again the peak of SSD, the dimple of C_1C_3, and the sign change of C_4 at $x = 0.474L$ clearly indicate the crack location. Because the first measurement point is actually about $0.1''$ to the right of the left clamped end, requiring $\theta_1 = 45°$ and matching the theoretical C_1 function of a clamped end shown in Table 1 with the curve-fitted C_1 curve indicates that the free end is at $x = -0.6''$, instead of $x = -0.1''$. In other words, the left end is not perfectly clamped, which was believed to be due to non-perfect contact between the two steel plates and the beam. The peak of SSD, the roughness of C_1C_3, and the sign change of C_4 around $x = 0$ also indicate a non-perfect boundary point. To improve the contact two pieces of duck tape were put between the two steel plates and the beam and a larger clamping force was applied, which resulted in the increase of the seventh peak on the average FRF to 2687.5 Hz. Fig. 17 shows the curve-fitted results obtained by processing the 2687.5 Hz ODS using $N = 5$ and $\Delta x = 3L/613$. The thin lines in Fig. 17(b)–(d) are obtained using $N = 5$ and $\Delta x = 6L/613$. Again the peak of SSD, the dimple of C_1C_3, and the sign change of C_4 at $x = 0.474L$ clearly indicate the crack location. Requiring $\theta_1 = 45°$ and matching the theoretical C_1 function of a clamped end with the curve-fitted C_1 curve indicates that the free end is at $x = -0.3''$, instead of $x = -0.1''$. In other words, the left end was still not perfectly clamped, which was believed to be due to the flexibility of the duck tape. If there is a crack at $x = 0$, the predicted left end will be

at $x < -0.3''$. However, the peak of SSD around $x = 0$ in Fig. 16(b) is eliminated in Fig. 17(b) because of a better contact. These tests show that even a perfectly clamped boundary condition is difficult to be realized in experiment.

Fig. 18 shows a free-clamped $23.94'' \times 0.743'' \times 0.188''$ aluminum beam with three cracks having a crack width $c = 0.039''$ and crack depths $e = 0.031''(= 0.16h)$, $e = 0.053''(= 0.28h)$, and $e = 0.025''(= 0.13h)$, respectively. Fig. 19 shows the results obtained using the BED method with $N = 5$ and $\Delta x = 2L/501$ to process the 1556.25 Hz ODS, and Fig. 20 is obtained using $N = 5$ and $\Delta x = 3L/501$. The thin lines in Figs. 19(b)–(d) and 20(b)–(d) are obtained using $N = 5$ and $\Delta x = 6L/501$. Figs. 19(a) and 20(a) show that it is difficult to locate the cracks, especially when the sliding-window length $2N\Delta x$ is large. On the other hand, the peaks of SSD and C_3, the dimples of C_1C_3, the sign changes of C_4, $\widehat{C}_3$, $\widehat{C}_4$ clearly indicate the three crack locations. Figs. 19(b)–(d) and 20(b)–(d) show that comparing damage location curves obtained using two different sliding-window lengths makes it easy to find damage locations. Although increase of the sliding-window length makes the peaks of SSD and the sign changes of C_4 clear, it reduces the dimples of C_1C_3. Hence, there should be an optimum sliding-window length for revealing damages. Experimental and numerical results showed that, if noise is small, a sliding-window length $(2N\Delta x)$ of $\lambda/4$ works best for locating and estimating cracks (Pai et al., 2003). However, because actual noise is usually unknown, it is

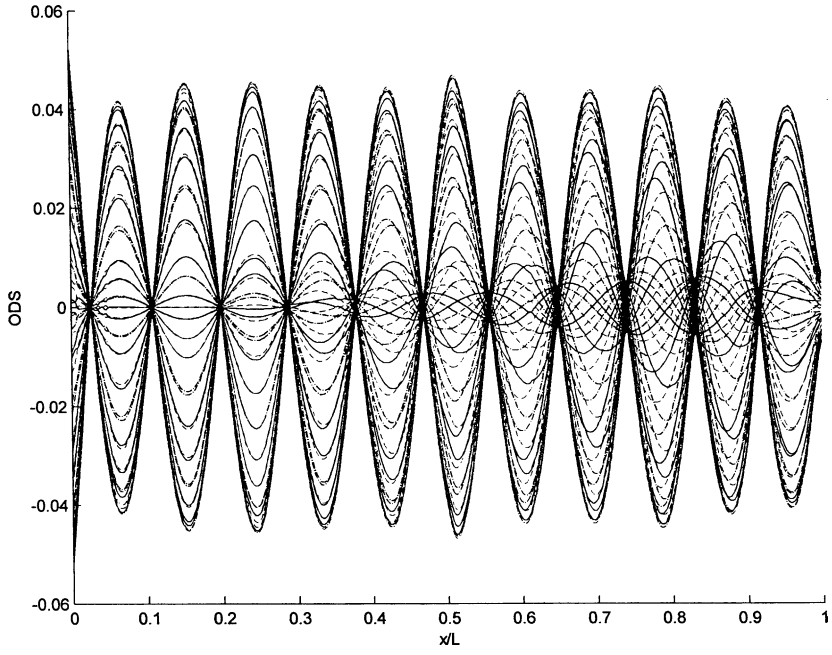

Fig. 21. The 3525.78 Hz traveling ODS.

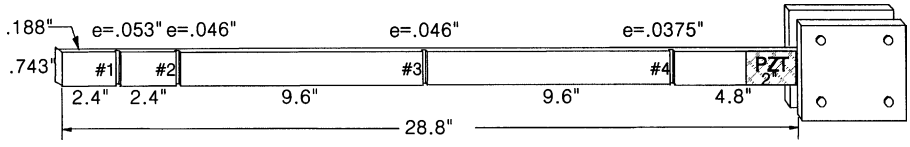

Fig. 22. A free-clamped aluminum beam with four cracks.

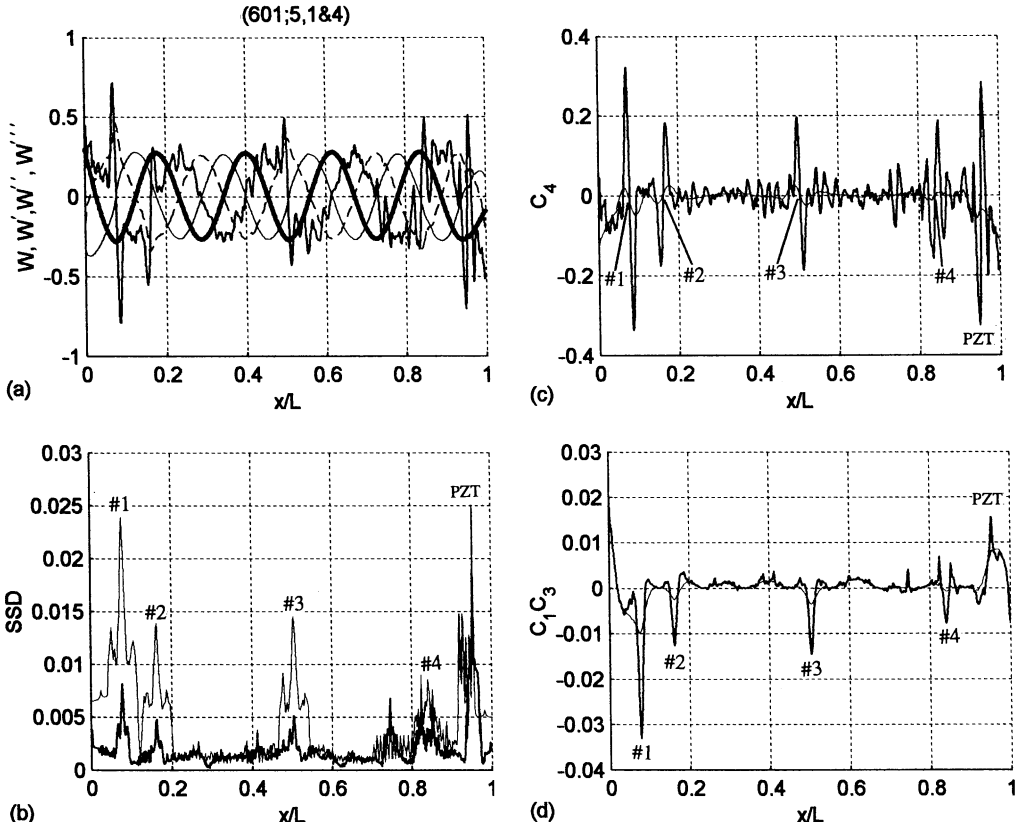

Fig. 23. Damage detection curves of the 1675 Hz ODS of the free-clamped $28.8'' \times 0.743'' \times 0.188''$ beam with four cracks using $N = 5$ and $\Delta x = 2L/601$: (a) W (dots), W'/β (thin line), W''/β^2 (broken line), and W'''/β^3 (thick line), (b) SSD, (c) C_4, and (d) C_1C_3.

better to process experimental data using at least two different sliding-window lengths. The peak of SSD around $x = 0$ is due to the first $6.06''$ beam segment was gradually distorted by twisting from $x = 6.06''$ to $x = 0$ by about 5°. The actual left end is at $x = -0.15''$, but requiring $\theta_1 = 45°$ and matching the theoretical C_1 function of a free end with the curve-fitted C_1 curve indicates that the free end is at $x = -0.09''$. This inaccuracy is due to the beam distortion. All the three cracks can be detected by the damage detection curves of this 1556.25 Hz ODS because each crack is close to a peak of the ODS. If there are cracks around the nodes of this ODS, they will be not revealed by the damage detection curves. Hence, at least two ODSs with peaks covering the whole beam need to be processed in order to reveal all possible defects.

An alternative approach is to examine just one traveling ODS because the peaks (and nodes) of a traveling ODS move. Eqs. (7) and (9) indicate that an easy way to have traveling ODSs is to create non-uniform distribution of damping properties. Two pieces of $6'' \times 0.743''$ 3M-DF-2552 damping foil were put between cracks #1 and #2 and cracks #2 and #3 shown in Fig. 18. The 3M-DF-2552 consists of a room temperature pressure sensitive viscoelastic polymer ($0.005''$ thick) on a dead soft aluminum foil ($0.01''$ thick), and the mass density is 0.17 lb/ft^2. Fig. 21 shows the 3525.78 Hz ODS at different time instants; it is apparently a traveling wave. Experimental results show that it is easier to obtain high-frequency traveling ODSs than low-frequency ones, and ODSs over the left beam segment without damping foil only show standing waves. We note that, although one can process a profile of a traveling ODS when its peaks move

close to the global nodes to detect damage around the global nodes, the damage detection curves are not clear because such a profile usually has a small amplitude with significant noise, as shown in Fig. 21.

Fig. 22 shows a free-clamped $28.8'' \times 0.743'' \times 0.188''$ aluminum beam with four cracks having a crack width $c = 0.039''$ and crack depths $e = 0.053''(= 0.28h)$, $e = 0.046''(= 0.24h)$, $e = 0.046''(= 0.24h)$, and $e = 0.0375''(= 0.20h)$, respectively. Fig. 23 shows the results obtained using the BED method with $N = 5$ and $\Delta x = 2L/601$ to process the 1675 Hz ODS. The thin lines in Figs. 23(b)–(d) are obtained using $N = 5$ and $\Delta x = 5L/601$. Again, the peaks of SSD, the dimples of C_1C_3, the sign changes of C_4 clearly indicate the four crack locations. The actual left end is at $x = -0.11''$, and requiring $\theta_1 = 45°$ and matching the theoretical C_1 function of a free end with the curve-fitted C_1 curve indicates that the free end is at $x = -0.13''$. This inaccuracy is due to crack #1 being close to $x = 0$. We note that, although cracks #1 and #2 are close to the left boundary point, the damage location curves SSD and C_1C_3 still show the damage locations clearly, and they are very similar to the numerical simulation results shown in Fig. 12.

The cracks that the BED method can locate and estimate has been experimentally shown to be cracks with a crack depth $e \geqslant 0.05h$ (Pai et al., 2003). However, we point out here that, if a crack is irregular or not perpendicular to the x-axis, the BED still works but the corresponding torsional deformation will affect the accuracy. Moreover, if the beam width is large, it is better to treat the structure as a two-dimensional (2D) structure. For 2D structures, a similar method can be derived for damage detection and boundary identification, which will be reported later.

7. Concluding remarks

A signal decomposition method for extracting boundary effects from an ODS is presented. The method processes an experimental ODS using a sliding-window least-squares curve-fitting technique to separate boundary and central solutions. The extracted boundary solutions can be used for finding damage locations, and the central solutions can be used for identifying actual boundary conditions. Numerical simulations and experimental results validate the proposed method for 1D structures.

Acknowledgements

This work is supported by the National Science Foundation through Grants CMS-9871288, CMS-9912482, and CMS-0120798. The support is gratefully acknowledged.

References

Doebling, S.W., Farrar, C.R., Prime, M.B., Shevitz, D.W., 1996. Damage identification and health monitoring of structural and mechanical systems from changes in their vibration characteristics: a literature review. Report No. LA-13070-MS, Los Alamos National Laboratory.

Doyle, J.F., 1989. Wave Propagation in Structures: An FFT-Based Spectral Analysis Methodology. Springer Verlag, New York.

Inman, D.J., 2001. Engineering Vibration, second ed. Prentice Hall, New Jersey.

Jin, S., Pai, P.F., 2000. Locating structural defects using operational deflection shapes. J. Intell. Mater. Syst. Struct. 11 (8), 613–630.

Lee, U., Jeon, D., 1999. Identification of non-ideal structural boundary conditions by using spectral element method. AIAA-99-1311.

Lee, U., Lee, J., 1997. Dynamic analysis of one- and two-dimensional structures using spectral element methods. In: Proceedings of the 6th International Conference on Recent Advances in Structural Dynamics, vol. 1. ISVR, University of Southampton, England, July.

Man, X.T.C., McClure, L.M., Wang, Z., Finch, R.D., 1994. Slot depth resolution in vibration signature monitoring of beams using frequency shift. J. Acoust. Soc. Am. 95 (4), 2029–2037.

Nayfeh, A.H., Mook, D.T., 1979. Nonlinear Oscillation. Wiley-Interscience, New York.

Pai, P.F., Jin, S., 2000. Locating structural damage by detecting boundary effects. J. Sound Vib. 231 (4), 1079–1110.
Pai, P.F., Lee, S.Y., 2003. Nonlinear structural dynamics characterization using a scanning laser vibrometer. J. Sound Vib. 264 (3), 657–687.
Pai, P.F., Young, L.G., 2001. Damage detection of beams using operational deflection shapes. Int. J. Solids Struct. 38 (18), 3161–3192.
Pai, P.F., Young, L.G., Lee, S.Y., 2003. A Dynamics-based method for crack detection and estimation. Struct. Health Monitor. 2, 5–25.
Thomson, W.T., 1949. Vibration of slender bars with discontinuities in stiffness. J. Appl. Mech. 16 (2), 203–207.
Wang, F., Chen, S., 1996. A method to determine the boundary condition of the finite element model of a slender beam using measured modal parameters. ASME J. Vib. Acoust. 118, 474–478.